Wing Structure Design for Flexible Delta-Type Wings at Low Speeds

Undergraduate Honors Thesis

Presented in Partial Fulfillment of the Requirements for the Degree of Bachelor of Science with Honors Research Distinction at The Ohio State University

By

Kegan C. Buchhop

The Ohio State University

2017

Professor Clifford A. Whitfield, Advisor

Dr. Matthew H. McCrink, Co-Advisor

Department of Mechanical and Aerospace Engineering

April 2017

Copyright by

Kegan Buchhop

2017

Abstract

Aerial reconnaissance plays a key role in gathering intelligence for the military. Unmanned aerial vehicles (UAVs) have proven that they can fulfill this role in a cost-effective manner. Furthermore, high-altitude UAVs fill this need well because they do not interfere with commercial air traffic. However, the effectiveness of these UAVs is subject to their range, endurance, and ease of deployment. High-altitude UAVs have an enhanced challenge of weight savings because there is less lift available at higher altitudes as air is less dense. Efforts to save weight for this class of UAV have proven catastrophic because they are designed for high-altitude flight and are susceptible to damage in turbulent areas of the lower atmosphere. To avoid this, it has been proposed to develop a tube-launched UAV deployed at the intended mission altitude. The wings of this UAV must be lightweight and easily folded and stowed in a tube. The wing must also be aerodynamically efficient to be a viable option for long-range aerial surveillance missions. Highly flexible polyimide wings fit these criteria; however, they have been experimentally shown to suffer losses in aerodynamic efficiency as a result of their flexibility. It has been shown in previous experiments that adding structure to the wing can increase aerodynamic efficiency. This research aims to determine ideal structure configuration to maximize the aerodynamic efficiency of such wings. This research will use wind tunnel testing to validate pressure distribution results obtained by Computational Fluid Dynamics. These pressures will then be translated to structural Finite Element models of wing concepts to determine an ideal configuration that maximizes aerodynamic efficiency while retaining low structural weight. Results are currently on-going, with the end goal being a drastic reduction in the cost associated with operating the high-altitude UAV.

Dedicated to my outstanding family and friends.

Acknowledgements

I would like to thank my advisor Dr. Clifford Whitfield for giving me the opportunity to carry out this research project. It was only with his guidance that this project was successful. Dr. Whitfield dedicated a large amount of time and effort to better me as a student and engineer, and for that I am deeply grateful. I would like to thank Dr. Matthew McCrink for his help and guidance on this research as well. I would also like to thank Mr. Jacob Allenstein and Mr. Gregory Rhodes for their help with experimental setup and data acquisition.

I would like to thank the machine shop staff at the Aerospace Research Center at Ohio State, specifically Josh Gueth and Ken Fout. Their training and assistance with machining was not only valuable for completing this research project, but it was beneficial for me as a student and engineer.

I would also like to thank the staff at NASA Marshall Space Flight Center in Huntsville, Alabama. The staff assisted me greatly with this research project during after-hours at my internship during the autumn of 2015. I greatly appreciate the time that Mark Black spent teaching me how to TIG weld. I am also very thankful that Stan McDonald took the time to waterjet some critical components of my research.

Finally, I would like to thank the Department of Mechanical and Aerospace Engineering at Ohio State for the opportunity to conduct research at the ARC and providing funding along the way.

Table of Contents

Abstract i

Acknowledgements iii

Table of Contents iv

List of Figures vi

List of Tables x

Nomenclature xi

Chapter 1: Introduction 1

1.1 Background 1

1.2 Motivation and Significance 3

1.3 Research Objectives 5

Chapter 2: Wind Tunnel Model Design and Fabrication 7

2.1 Model Design 7

2.2 Model Fabrication 10

Chapter 3: Experimental Facilities, Equipment, and Uncertainty Analysis 12

3.1 Experimental Facilities 12

3.2 Pressure Measurements 14

3.3 Data Acquisition 15

3.4 Measurement Uncertainty Analysis 16

Chapter 4: Wind Tunnel Testing, Results, and Discussion 17

4.1 Test Matrix..... 17

4.2 Test Results - 30-Degree Model..... 17

4.3 Test Results - 60-Degree Model..... 20

Chapter 5: FEM Analysis of Wing Structure Design.....24

5.1 Wing Structure Designs 24

5.2 FEM Setup 25

5.3 Results and Discussion 27

Chapter 6: Conclusions and Future Work 30

References 32

Appendix 33

List of Figures

Figure 1: Conceptual Design of UAV [2] 3

Figure 2: Flexible Wing Model | Λ = 30° [3] 3

Figure 3: Wind Tunnel Model with Single Rib | Λ = 30° [3] 4

Figure 4: Top View of Λ = 30° Port Configuration 8

Figure 5: Top View of Λ = 60° Port Configuration 9

Figure 6: Λ = 30-Degree Rigid Model 9

Figure 7: Λ = 60-Degree Rigid Model 9

Figure 8: Model Assembly - Leading edge Spar to Flat Plate 10

Figure 9: Completed 30° Model 11

Figure 10: Completed 60° Model 11

Figure 11: Chord as a Function of Wing Span (Λ = 30° Left, Λ = 60° Right) 12

Figure 12: Wind Tunnel Sting Mount (0 Degrees AOA Left, 16 Degrees AOA Right) 13

Figure 13: Pressure Scanner (Background) and Pressure Transducers 14

Figure 14: NetScanner 90DB Distribution Box [6] 15

Figure 15: 60° Wind Tunnel Model Setup 17

Figure 16: Upper Surface Pressure Distribution | 30-Degree Model | α = 0° 18

Figure 17: Upper Surface Pressure Distribution | 30-Degree Model | α = 5° 18

Figure 18: Upper Surface Pressure Distribution | 30-Degree Model | α = 10° 19

Figure 19: Upper Surface Pressure Distribution | 30-Degree Model | α = 15° 19

Figure 20: Flow Field Over Delta Wing [7] 20

Figure 21: Upper Surface Pressure Distribution | 60-Degree Model | α = 0° 21

Figure 22: Upper Surface Pressure Distribution | 60-Degree Model | α = 5° 21

Figure 23: Upper Surface Pressure Distribution | 60-Degree Model | α = 10° 22
Figure 24: Upper Surface Pressure Distribution | 60-Degree Model | α = 15° 22
Figure 25: a) 60° Delta Wing at α = 5° b) 60° Delta Wing at α = 15° [7] 23
Figure 26: Pressure Difference Distribution | α = 10° Left, α = 15° Right [3] 24
Figure 27: Top View of 10-Foot Models Under Investigation 25
Figure 28: Boundary Conditions Applied to Three Rib Model 26
Figure 29: Displacement [in.] | Three Rib Model | 15° AOA 27
Figure 30: Displacement [in.] | 45/15 Model | 15° AOA 27
Figure 31: Displacement [in.] | 30/30 Model | 15° AOA 28
Figure 32: Displacement [in.] | 15/45 Model | 15° AOA 28
Figure 33: Λ = 30° | Upper Surface | α = 0° | Run 1 34
Figure 34: Λ = 30° | Lower Surface | α = 0° | Run 1 34
Figure 35: Λ = 30° | Upper Surface | α = 0° | Run 2 35
Figure 36: Λ = 30° | Lower Surface | α = 0° | Run 1 35
Figure 37: Λ = 30° | Upper Surface | α = 5° | Run 1 36
Figure 38: Λ = 30° | Lower Surface | α = 5° | Run 1 36
Figure 39: Λ = 30° | Upper Surface | α = 5° | Run 2 37
Figure 40: Λ = 30° | Lower Surface | α = 5° | Run 2 37
Figure 41: Λ = 30° | Upper Surface | α = 10° | Run 1 38
Figure 42: Λ = 30° | Lower Surface | α = 10° | Run 1 38
Figure 43: Λ = 30° | Upper Surface | α = 10° | Run 2 39
Figure 44: Λ = 30° | Lower Surface | α = 10° | Run 2 39
Figure 45: Λ = 30° | Upper Surface | α = 15° | Run 1 40
Figure 46: Λ = 30° | Lower Surface | α = 15° | Run 1 40
Figure 47: Λ = 30° | Upper Surface | α = 15° | Run 2 41
Figure 48: Λ = 30° | Lower Surface | α = 15° | Run 2 41

Figure 49: Λ = 60° | Upper Surface | α = 0° | Run 1 42
Figure 50: Λ = 60° | Lower Surface | α = 0° | Run 1 42
Figure 51: Λ = 60° | Upper Surface | α = 0° | Run 2 43
Figure 52: Λ = 60° | Lower Surface | α = 0° | Run 2 43
Figure 53: Λ = 60° | Upper Surface | α = 5° | Run 1 44
Figure 54: Λ = 60° | Lower Surface | α = 5° | Run 1 44
Figure 55: Λ = 60° | Upper Surface | α = 5° | Run 2 45
Figure 56: Λ = 60° | Lower Surface | α = 5° | Run 2 45
Figure 57: Λ = 60° | Upper Surface | α = 10° | Run 1 46
Figure 58: Λ = 60° | Lower Surface | α = 10° | Run 1 46
Figure 59: Λ = 60° | Upper Surface | α = 10° | Run 2 47
Figure 60: Λ = 60° | Lower Surface | α = 10° | Run 2 47
Figure 61: Λ = 60° | Upper Surface | α = 15° | Run 1 48
Figure 62: Λ = 60° | Lower Surface | α = 15° | Run 1 48
Figure 63: Λ = 60° | Upper Surface | α = 15° | Run 2 49
Figure 64: Λ = 60° | Lower Surface | α = 15° | Run 2 49
Figure 65: Boundary Conditions Applied to 45/15 Model 50
Figure 66: Boundary Conditions Applied to 30/30 Model 50
Figure 67: Boundary Conditions Applied to 15/45 Model 50
Figure 68: von Mises Stress | 45/15 Model | 15° AOA 51
Figure 69: von Mises Stress | 30/30 Model | 15° AOA 51
Figure 70: von Mises Stress | 15/45 Model | 15° AOA 51
Figure 71: von Mises Stress [Pa] | 45/15 Model | 10° AOA 52
Figure 72: von Mises Stress [Pa] | 30/30 Model | 10° AOA 52
Figure 73: von Mises Stress [Pa] | 15/45 Model | 10° AOA 52
Figure 74: Displacement [in] | 45/15 Model | 10° AOA 53

Figure 75: Displacement [in] | 30/30 Model | 10° AOA 53

Figure 76: Displacement [in] | 15/145 Model | 10° AOA 53

List of Tables

Table 1: Flat Delta-Type Wing Performance Comparison | Λ = 60° [3] 4

Table 2: Rib Effects to Aerodynamic Characteristics | Λ = 30° [3] 5

Table 3: Tap Locations | Λ = 30° 8

Table 4: Tap Locations | Λ = 60° 8

Table 5: Equipment Specification Summary 15

Table 6: Material Properties of High Modulus Carbon Fiber 26

Table 7: Wind Tunnel Test Parameters 33

Nomenclature

Symbol

b	Span
c	Chord
y	Local Position in Span-wise Direction
$C_{L\alpha}$	Lift Curve Slope
$C_{L,Max}$	Maximum Lift Coefficient
C_N	Coefficient of Normal Force
C_P	Coefficient of Pressure
L/D	Lift to Drag Ratio
L/D_{MAX}	Maximum Lift to Drag Ratio
MAC	Mean Aerodynamic Chord
N	Normal Force
P_amb	Ambient Pressure
S	Wing Area
T_amb	Ambient Temperature
V	Free Stream Velocity
α	Angle of Attack
Λ	Leading Edge Sweep
ρ	Density of Free Stream

Abbreviations

AOA	Angle of Attack
ARC	Aerospace Research Center

CAD	Computer Aided Design
FEM	Finite Element Method
HALE	High-Altitude, Long Endurance
TIG	Tungsten Inert Gas
UAV	Unmanned Aerial Vehicle

Chapter 1: Introduction

1.1 Background

High altitude, long endurance (HALE) unmanned aerial vehicles (UAVs), also referred to as Tier II+ UAVs by the Air Force, are required to fly between 60,000 and 70,000 feet. These aircraft usually fly at less than 300 knots and are required to loiter for a long period of time. By nature, the air is much less dense at this altitude than at sea level (a reduction of about 95% on a standard day). Lift, which is directly proportional to air density, is greatly hindered because there is simply not a lot of air to work with at this altitude. Therefore, the necessity for the aircraft to have a large wing area, high aerodynamic efficiency, and low weight is paramount.

In an effort to reduce the weight of HALE class aircraft, some manufacturers have pushed the limits of structure used to support the wing. This has proven to be catastrophic in some cases, such as the prototype 2001 Helios HPO3 aircraft designed by NASA Dryden Flight Research Center (now NASA Armstrong Flight Research Center) and AeroVironment, Inc. The Helios program was a proof-of-concept, propeller-driven, flying wing with two configurations. The first configuration, designated HP01, was designed to run on batteries and highly efficient solar cells placed on the upper surface of the 247 foot wingspan. HP01 set the record for highest sustained horizontal flight of a winged aircraft at an altitude of 96,863 feet. The second configuration, designated HP03, was designed specifically for long-duration flight. It incorporated solar cells to power the vehicle during the day and a hydrogen-air fuel cell system for use at night. The aircraft design used wing dihedral, engine power, elevator control surfaces, and stability augmentation and control systems to provide aerodynamic stability and control.

In June of 2003, HP03-2 took off from a Naval Missile Range in Kauai, Hawaii. The weather in the area appeared to be well within the flight envelope. The aircraft was ascending on the downwind side

of the extinct volcano when it encountered turbulence. The wing dihedral grew much larger than normal and mild pitch oscillations began. This behavior dampened out for a short period of time before more turbulence was encountered. The wing rapidly progressed into a persistent high dihedral that caused the aircraft to go into a very divergent pitch mode. This caused the aircraft to exceed the nominal flight speed and led to dynamic pressures that exceeded the designed flight loading. The vehicle structure underwent catastrophic failure and the aircraft crashed into the Pacific, a costly mission failure.

Though it is debatable whether the vehicle was properly designed for its given mission profile, it is apparent that it is difficult to design a HALE class aircraft to operate safely in the lower regions of the atmosphere. Since high dynamic pressures associated with turbulence in the lower atmosphere are seemingly problematic, it is easily pointed out that the turbulence can be avoided by eliminating the ascent and descent through these regions altogether. An interesting solution to this problem is deploying the UAV directly at operating altitude with another aircraft, a high-altitude balloon, or a rocket. A foldable UAV would be beneficial in this case because it could be launched or deployed from a tube to save space.

Tube-launched UAV's in use today usually implement some sort of telescoping or rigid pivoting wing. The issue in this scenario is that the wing area is limited to the size of the deployment tube. A unique concept that challenges this design assumption is a delta-type planform utilizing a flexible material, such as Polyimide film, as the main lifting surface. The main advantage of a flexible delta-type wing is that it has the potential for many packing options while maintaining low overall weight. For purposes of portability, the delta-type wing shape allows for a system of spars and hinges to deploy the wing from a single fuselage location. This concept is termed "parawing" because the lifting surface combines the properties of a traditional wing and that of a parachute. This concept was first investigated for space capsule recovery by Francis Rogallo, a NASA engineer, in the 1950's. For UAV operations, the parawing offers unique solutions for portability and high altitude deployment. Such a vehicle could be designed to avoid low level turbulence while also eliminating the need to assemble/disassemble the vehicle for transportation and deployment purposes. The aircraft concept, designed by Clifford Whitfield

of Whitfield Aerospace LLC, is shown below in Figure 1. This design is protected under U.S. Patent 9272783 B2, 2016 by J. Pearson and C. Whitfield.[1,2]

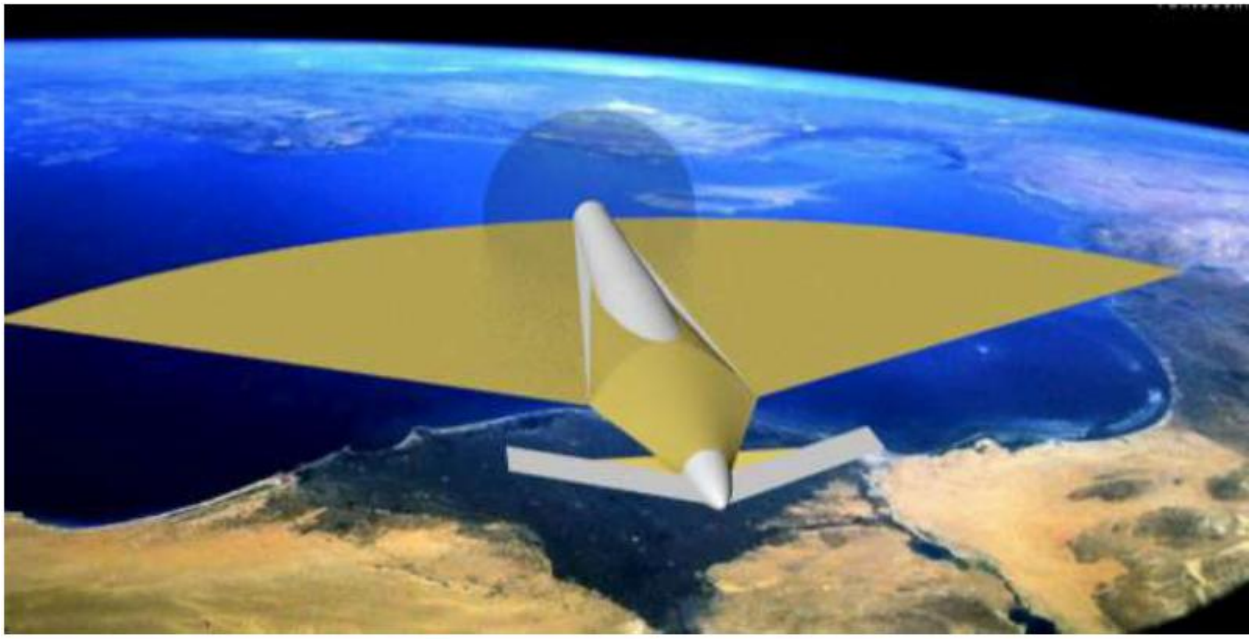

Figure 1: Conceptual Design of UAV [2]

1.2 Motivation and Significance

Designing a UAV with a flexible delta-type wing presents many challenges. Previous research by Whitfield has shown that a flexible delta-type wing suffers in aerodynamic performance compared to a rigid delta-type wing.[3] An image of the flexible model and the results of this test are shown below in Figure 2 and Table 1 respectively.

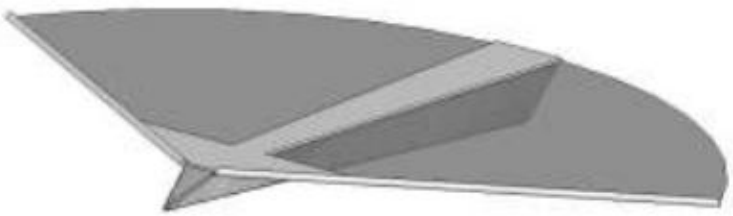

Figure 2: Flexible Wing Model | Λ = 30° [3]

Table 1: Flat Delta-Type Wing Performance Comparison | Λ = 60° [3]

Type	C_{Lmax}	α	$C_{L\alpha}$	L/D
Rigid Wing	1.278	30	0.051	14.5
Polyimide Film	1.135	30	0.047	8.8

The results show that both models have a similar $C_{L,Max}$ at 30 degrees angle of attack. Their lift curve slopes are also comparable. The difference lies with the lift to drag ratio. The flexible wing only gets about 40% of the L/D of the rigid model. Knowing that L/D is equal to C_L/C_D, and observing that the $C_{L,Max}$ is similar between models, it is clear that the reduction in L/D is caused by excessive drag on the flexible wing. It was hypothesized that this reduction in L/D was due to the flexible material billowing as a result of large pressure gradients on the flexible wing surface.

Whitfield addressed this issue through investigating how adding internal structure to the flexible wing affects aerodynamic performance. A systemic approach of having the ribs emanate from the leading edge root, similar to the leading edge spar, split the flexible wing into equal areas. The number of ribs was then varied between tests to see how incrementally adding structure to the flexible wing would affect performance. This began with one rib splitting the 30-degree leading edge sweep wing into two equal areas (setup shown in Figure 3 below), and ended with seven ribs splitting the wing into eight equal areas. The results are shown below in Table 2.

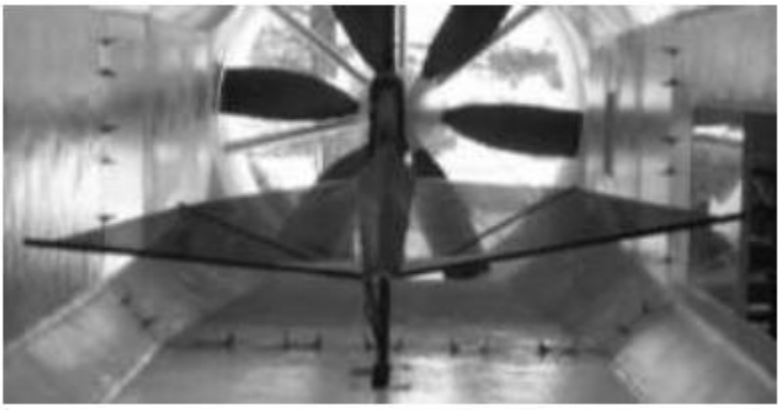

Figure 3: Wind Tunnel Model with Single Rib | Λ = 30° [3]

Table 2: Rib Effects to Aerodynamic Characteristics | Λ = 30° [3]

Ribs	Lift Characteristics			Maximum Aerodynamic Efficiency		
	$C_{L,Max}$	α (deg)	$C_{L\alpha}$	L/D	C_L	α (deg)
0	0.62	20	0.038	6.4	0.25	8
1	1.05	16	0.065	9.8	0.51	8
3	1.17	18	0.077	14.1	0.66	8
7	0.98	16	0.078	11.7	0.44	6

These results show that adding structure increases L/D drastically; however, as the number of ribs increases from three to seven, the L/D actually decreases. This shows that there is an ideal balance of wing structure that, when surpassed, has no additional aerodynamic benefit. The takeaway is that an understanding of how adding structure benefits aerodynamic performance is needed. A better understanding of the pressure distribution on the wing will be useful for indicating where structural additions will have the most aerodynamic benefit. The wing structure can then be designed in such a way that it adds the smallest amount of weight to the overall design.

1.3 Research Objectives

The present research aims to experimentally determine the pressure distribution on rigid delta-type wings of two distinct leading edge sweep angles. The selected leading edge sweep angles will be 30° and 60° because they have drastically different aerodynamic qualities, and the current design of the UAV has the ability to deploy the wing in either configuration. Computer-aided design (CAD) will be utilized to aid in the design the models prior to fabrication. The methods for designing and fabricating these models will be discussed in Chapter 2. Once fabricated, both models will be investigated in a 3' x 5' subsonic wind tunnel at the Ohio State Aerospace Research Center (ARC). The experiments will be run using the full-scale Reynolds number at angles of attack ranging from 0° to 15°.

Concurrently, FEM analysis of multiple wing structure designs for a 10-foot root chord model will be conducted. Each analysis will be performed on the 30° sweep model only because this

configuration is expected to see the highest stresses and deflections. These preliminary designs differ from the designs discussed by Whitfield [3], and need to be investigated to understand how the wing structure will behave during flight. This ensures structural deflections are reasonable and that the wing structure will not be compromised.

Chapter 2: Wind Tunnel Model Design and Fabrication

2.1 Model Design

The wind tunnel models were designed with suggestions from *Low-Speed Wind Tunnel Testing* in mind.[4] One rule of thumb is that the models should be designed such that the wingspan is less than 80% of the width of the wind tunnel. This meant that the maximum wingspan of the models should be 4 feet or less. Instead of scaling each model based on the leading edge sweep, the models were based on a 0-degree leading edge sweep model with a 4-foot wingspan. This effectively sets a root chord of 2 feet for each model and allows each model, regardless of leading edge sweep angle, to use the same wind tunnel mounting architecture.

It is also suggested that pressures should be measured at several span locations with taps located at 0.125, 2.5, 5, 10, 15, 20, 30, 40, 50, 60, 70, 80, 95, and 100% chord on both upper and lower surfaces.[4] However, the models are limited to a total of 68 ports (34 on the upper surface and 34 on the lower surface) due to the limited number of pressure transducers available. This in mind, the pressure taps are placed strategically such that they are concentrated in locations with large anticipated pressure gradients. The locations of the taps for each model are shown below in Table 3 and Table 4. Top views of the models and their port locations are also shown in

Figure 4 and Figure 5.

As mentioned in Chapter 1, models with leading edge sweep angles of 30° and 60° were selected because they posses drastically different aerodynamic qualities. The vehicle also has the ability to be deployed in either configuration, exhibiting the need for understanding the pressure distribution in both scenarios. The leading edge spar in use on both models follows the same diameter spar as used by Whitfield.[3] The top of the spar is mounted flush with the top of the model, similar to how the flexible

material would be configured on the full-scale UAV. Each model is also mounted to the same fuselage spike used by Whitfield.[3] These models are shown below in Figure 6 and Figure 7.

Table 3: Tap Locations | Λ = 30°

	Span Location (% Halfspan)	Number of Ports	Tap Locations (% Chord)
Λ = 30°	10	10	2.5, 5, 10, 15, 20, 30, 45, 60, 75, 90
	20	6	5, 10, 20, 40, 70, 100
	40	6	5, 10, 20, 40, 70, 100
	60	6	5, 10, 20, 40, 70, 100
	80	6	5, 10, 20, 40, 70, 100

Table 4: Tap Locations | Λ = 60°

	Span Location (% Halfspan)	Number of Ports	Tap Locations (% Chord)
Λ = 60°	17.5	9	2.5, 5, 10, 15, 20, 30, 50, 75, 90
	25	8	5, 10, 15, 22.5, 30, 40, 60, 80
	35	8	5, 10, 15, 22.5, 30, 40, 70, 100
	55	5	10, 25, 40, 70, 100
	80	4	25, 40, 70, 100

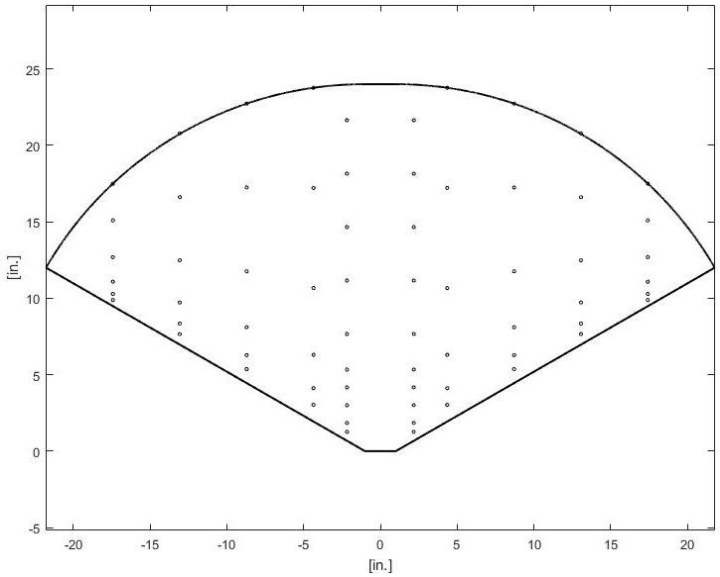

Figure 4: Top View of Λ = 30° Port Configuration

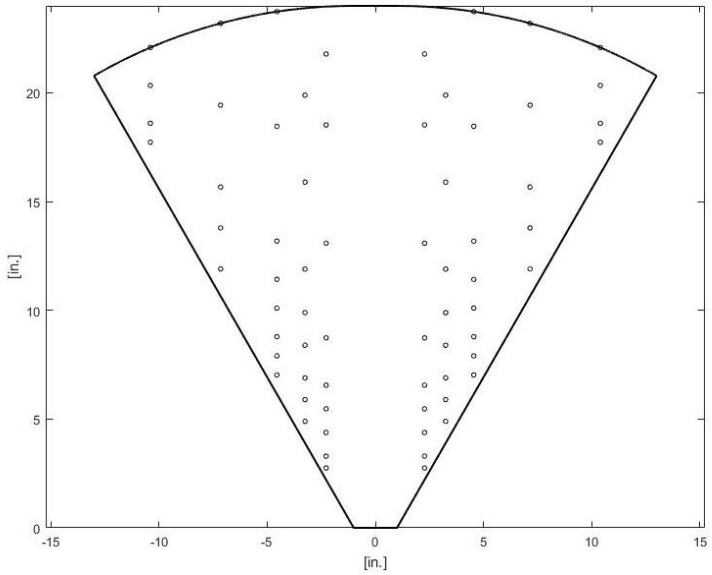

Figure 5: Top View of Λ = 60° Port Configuration

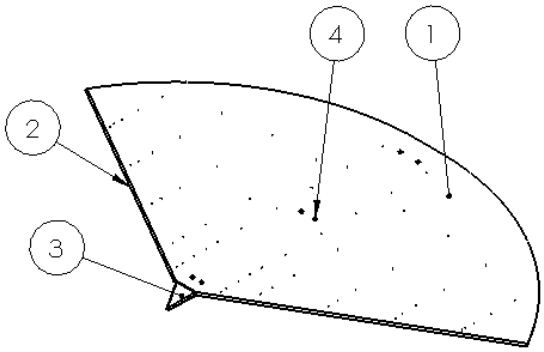

ITEM NO.	PART NUMBER	QTY.
1	Rigid Wing	1
2	0.25" Spar	2
3	Fuselage	1
4	8-32 Screw	6

Figure 6: Λ = 30-Degree Rigid Model

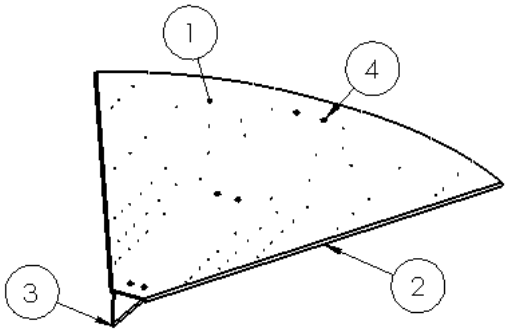

ITEM NO.	PART NUMBER	QTY.
1	Rigid Wing	1
2	0.25" Spar	2
3	Fuselage	1
4	8-32 Screw	6

Figure 7: Λ = 60-Degree Rigid Model

2.2 Model Fabrication

Stainless steel was the chosen material for fabricating the models. Stainless was selected because it was readily available at the time of fabrication. It also possesses great TIG welding qualities and does not rust or corrode when exposed to humid air (such as the Ohio climate).

The rigid flat plates were drawn in CAD and exported to a waterjet in a machine shop at NASA's Marshall Space Flight Center. The holes for the pressure taps, along with the outline of the wing, were cut with an accuracy of +/- 0.003". This process was chosen because it was much simpler than machining the holes for the taps on a 3 axis mill. This choice cut the manufacturing time for each flat plate down from approximately 5 hours per model to 25 minutes per model.

To make the assembly of the models easier, an 1/8" notch was machined into the top of both leading edge spars and the underside of the leading edge of the flat plate. This allows each part to butt up against one-another. Once in place the assembly was TIG welded together. This process is depicted below in Figure 8. After the entire leading edge was welded, the excess weld material was ground down and sanded smooth. The upper and lower surfaces of the wing were then sanded and polished.

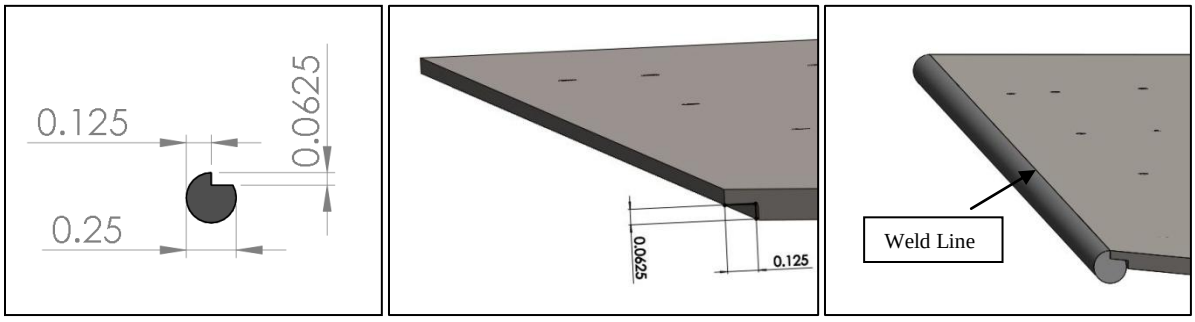

Figure 8: Model Assembly - Leading edge Spar to Flat Plate

The taps were made of 1/16" OD, 1/32" ID stainless steel tubing cut to 1.5" lengths. The tubes were bent to 90° elbows to run Tygon tubes parallel to the surface of the wing. The stainless tubes were then glued in place with J.B. Weld. Once cured, the openings of the taps were ground flush with the surface of the wing, deburred, and then checked for clogs. Tygon tubes were then pressed onto the free

end of the stainless tubes and run down to the pressure transducers at the back end of the model. The completed models are shown below in Figure 9 and Figure 10.

Figure 9: Completed 30° Model

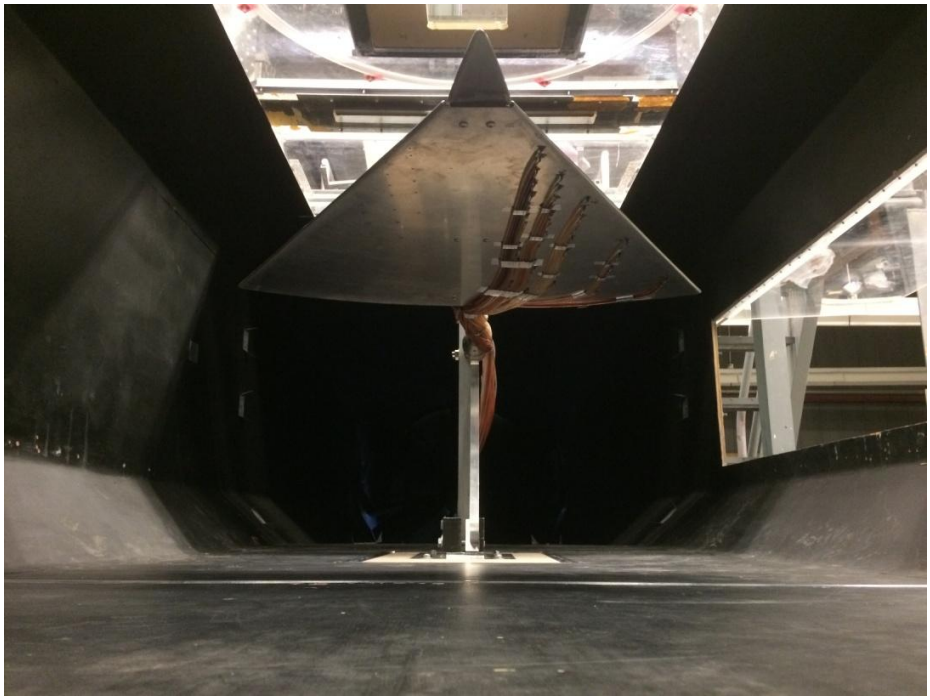

Figure 10: Completed 60° Model

Chapter 3: Experimental Facilities, Equipment, and Uncertainty Analysis

3.1 Experimental Facilities

Experimental testing was conducted at the low-speed subsonic wind tunnel facility at the ARC. The wind tunnel facility has a 3' x 5' test section. The tests were conducted at a Reynolds Number of 500,000 based on the wing mean aerodynamic chord. The mean aerodynamic chord is calculated from Equation 1below where S is the total wing area, b is the wingspan, c is the chord as a function of span, and y is a given location along the span. The chord as a function of span is shown below in Figure 11.

Equation 1: MAC

$$MAC = \frac{2}{S}\int_{0}^{b/2} c^2 dy$$

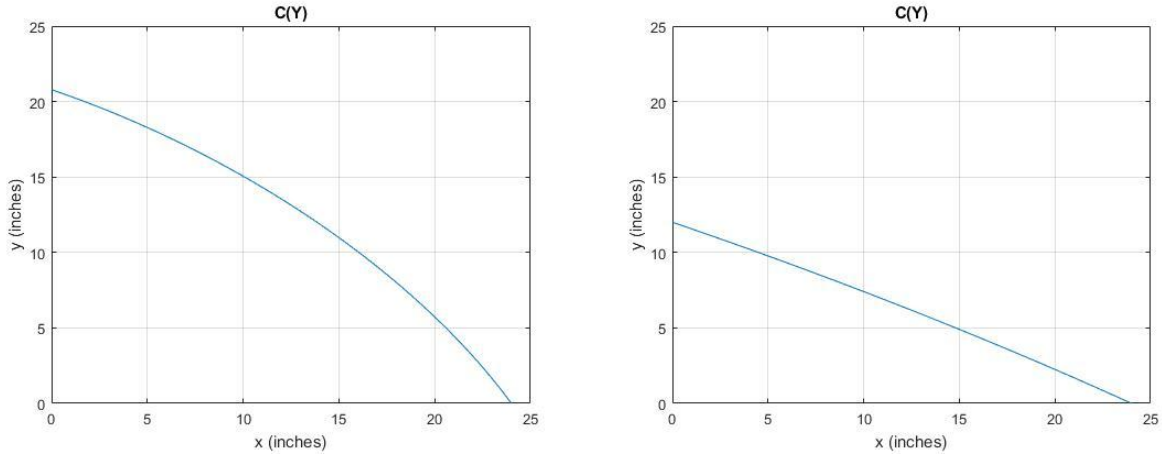

Figure 11: Chord as a Function of Wing Span (Λ = 30° Left, Λ = 60° Right)

The important take away from this calculation is that MAC changes slightly based on the leading edge sweep angle. The MAC of the 30-degree model is 73.5% of the root chord, whereas the MAC of the 60-degree model is 68.2% of the root chord. This was taken into account for setting the tunnel velocity.

The angle of attack was adjusted between 0 and 15 degrees in approximately 5 degree increments. This was done using a custom sting mount fabricated in-house. The sting holds the model centered in the test section and has the ability to adjust between 0 and 30 degrees AOA in 2 degree increments. The mount also has the ability to attach to a six-component internal strain gauge or an adapter. This mount is shown below in Figure 12.

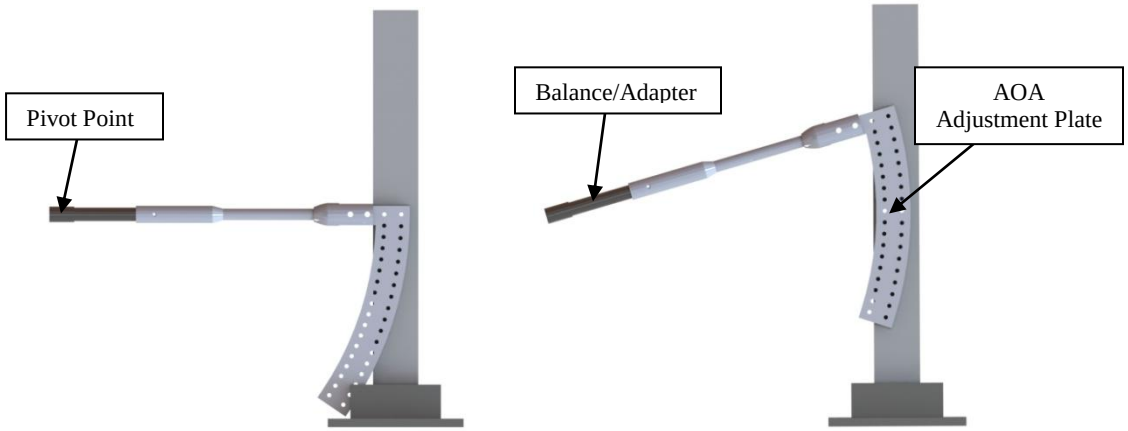

Figure 12: Wind Tunnel Sting Mount (0 Degrees AOA Left, 16 Degrees AOA Right)

Although the angle of attack can be adjusted in approximately 2 degree increments, the true angle of attack was measured using a military-grade gunner's quadrant accurate to 0.2 mils or 0.01 degrees.

Wind tunnel airspeed was measured using a Model 8350 VelociCalc Air Velocity Meter. Due to the unsteady nature of the low speed wind tunnel, the wind speed was set as close to desired airspeed as possible and then the actual tunnel velocity was collected with the air velocity meter. The meter measures standard velocity referenced to a standard day. To calculate the actual velocity, the following equation is used to correct for non-standard density.[5]

Equation 2: Actual Velocity

$$\boldsymbol{Actual\ Velocity} = (\boldsymbol{Standard\ Velocity})\ \boldsymbol{x}\ \frac{(\boldsymbol{460 + T\_amb})}{(\boldsymbol{460 + 70})}\ \boldsymbol{x}\ \frac{\boldsymbol{14.7}}{\boldsymbol{P\_amb}}$$

3.2 Pressure Measurements

The pressure taps were connected to five individual pressure scanners via Tygon tubing. Each of the Measure Specialties pressure scanners were fitted with 16 pressure transducers. The transducers ranged from 1 PSID to 5 PSID, based on availability.

Figure 13: Pressure Scanner (Background) and Pressure Transducers

With a small pressure differential, a low PSID rated transducer is desirable for more accurate data as the accuracy is a function of the transducer's full scale output. Each pressure scanner was connected to a NetScanner 90DB Distribution Box. In addition to supplying the necessary electrical power to the pressure scanners, the distribution box also relays the signals from the scanners back to the computer via Ethernet connection.

Figure 14: NetScanner 90DB Distribution Box [6]

Table 5 below gives a detailed overview of the equipment used and the accuracy associated with each pressure transducer.

Table 5: Equipment Specification Summary

Pressure Measurement Equipment
- Measurement Specialties Pressure Scanner NetScanner System 9116
- Range: 1 PSID, 5 PSID
- Pressure Inputs per Scanner: 16
- Measurement Resolution: +/-0.003% F.S.
- Static Accuracy (after re-zero): +/- 0.05% F.S. for 5 PSID Transducer +/- 0.15% F.S. for 1 PSID Transducer

3.3 Data Acquisition

A central computer was used to process all data. The computer runs Windows XP 32 bit and included a National Instruments SCXI-1102 Thermocouple/Voltage Input Module and a National Instruments BNC/TC-2095. Voltage inputs from the pressure transducers previously mentioned in Section 3.2 are processed by these modules. Data was acquired using LabVIEW 11.0. The program runs at 500 HZ and averages the measured pressures over a 5 second interval to output a given pressure reading for each port.

3.4 Measurement Uncertainty Analysis

Each of the five Measurement Specialties pressure scanners contained 16 transducers for a total of 80 pressure transducers. As seen from Table 5, the 5 PSID transducers have a static accuracy of 0.05% full scale and 0.15% full scale for the 1 PSID transducers. The accuracies of the instrumentation measurements were used to determine the uncertainty values expected.

An uncertainty analysis regarding experimental measurements was conducted to understand the total experimental equipment error associated with the system. The total error is composed of both bias and precision error. Bias error is the constant error associated with a given system. This is the error most closely related to the accuracy of the measurements. Precision error is the difference between experimental values under unchanged testing conditions. An uncertainty analysis is designed to bound the accuracy of the collected data. Measurement uncertainty analysis provides investigators with test validation, helps identify the corrective action needed to achieve their test objective(s), helps reduce errors, and helps stay in compliance with agreements and contracts.[6]

The 1 PSID pressure transducer is rated to 0.15% full scale. The inaccuracy associated with each measurement is calculated by dividing the percent accuracy by 100 and then multiplying by the full scale rating. This bounds the inaccuracy to +/- 0.0015 PSID. Therefore, if a pressure measurement recorded using the 1 PSID transducer is -0.0314, the error bars would be between -0.0329 and -0.0299 psi. The 5 PSID pressure transducer is rated to 0.05% full scale and is bounded by +/- 0.0025 PSID. Therefore, if the same -0.0314 psi pressure measurement is recorded with the 5 PSID transducer, the bounds would be -0.0339 and -0.0289 psi. The pressure transducers collect data at a sample rate of 500 Hz over a five second time span. The values are then averaged and exported to an excel sheet. A MATLAB script was used to read in the values from the excel sheet and map the pressure distribution across the upper and lower surfaces of the wing.

Chapter 4: Wind Tunnel Testing, Results, and Discussion

4.1 Test Matrix

As mentioned previously, both models were tested at a Reynolds Number of 500,000. The angles of attack ran from 0 degrees to 15 degrees in 5 degree increments. The tests at each angle of attack were run twice for repeatability checks. This gave a total of 8 tests per model, or 16 total runs. The setup is shown below in Figure 15.

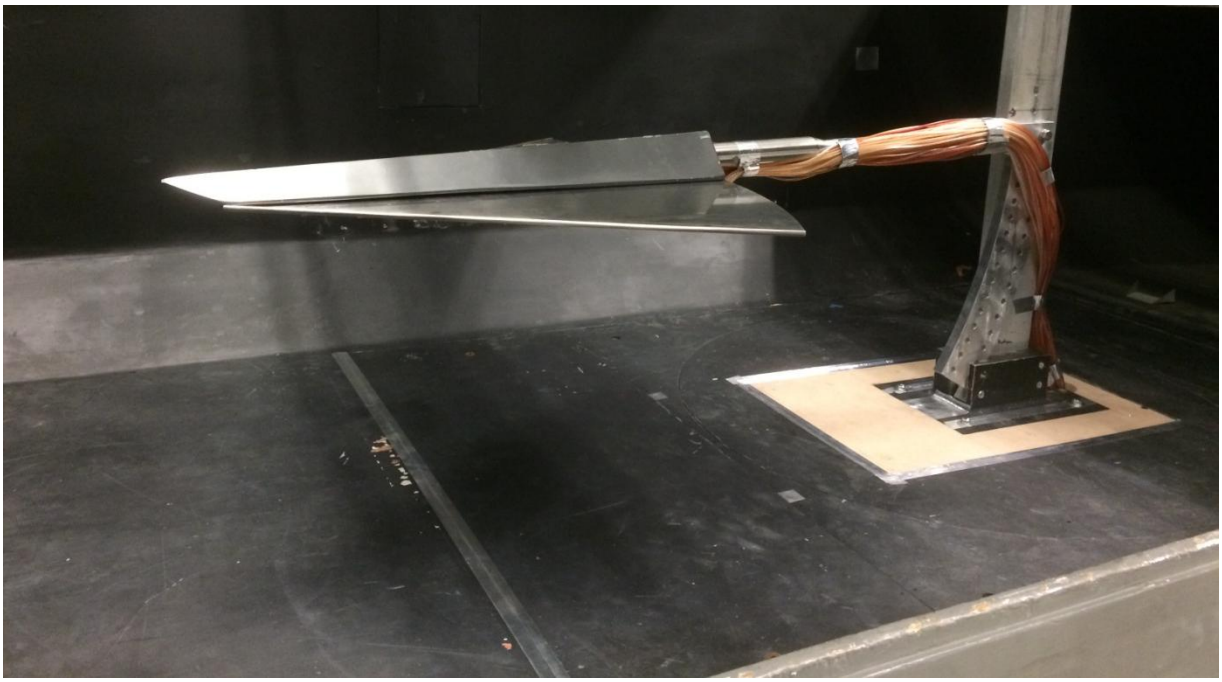

Figure 15: 60° Wind Tunnel Model Setup

4.2 Test Results - 30-Degree Model

Only half of the model has pressure ports on the upper surface of the wing. The other half of the wing has pressure ports on the lower surface. The full pressure distribution was then approximated through symmetry about the midline of wing. The pressure distribution was interpolated between ports

using MATLAB's built-in 'natural' interpolation method that combines linear and cubic interpolation. It should be noted that the regions of interpolation do not reflect the true pressure at that location. The interpolation is just used to give a general idea of how pressure is distributed along the surface of the wing. The readings from the pressure taps are the only true pressure measurements on the wing.

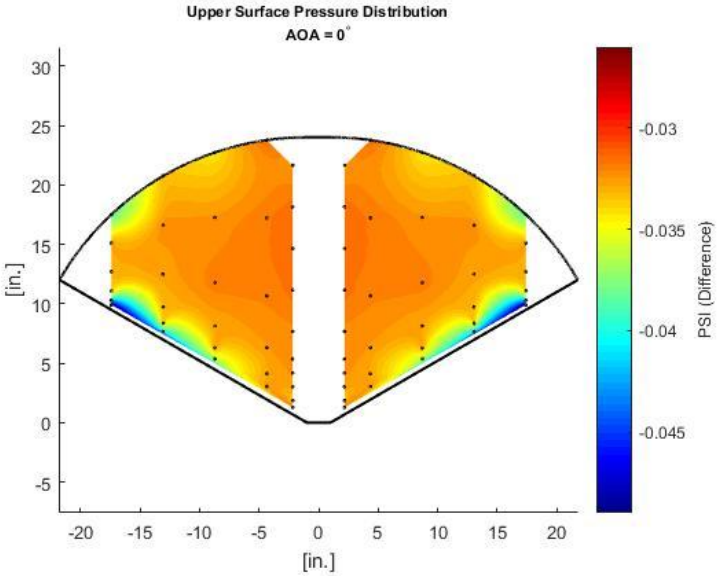

Figure 16: Upper Surface Pressure Distribution | 30-Degree Model | $\alpha = 0°$

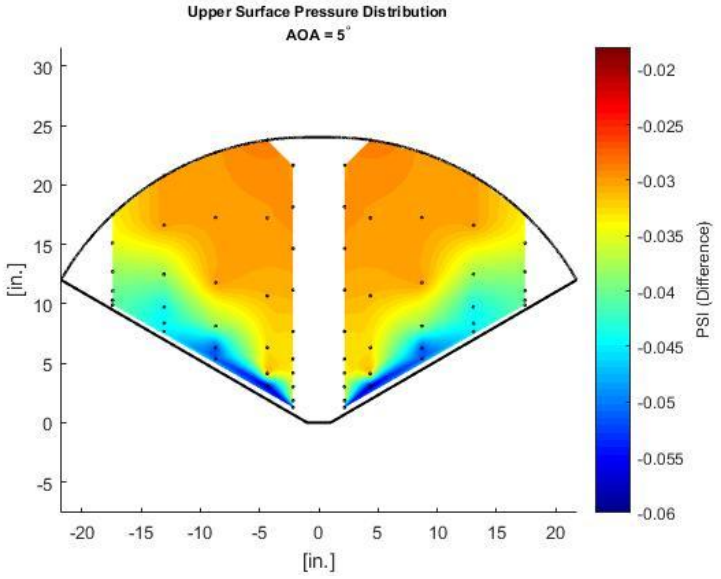

Figure 17: Upper Surface Pressure Distribution | 30-Degree Model | $\alpha = 5°$

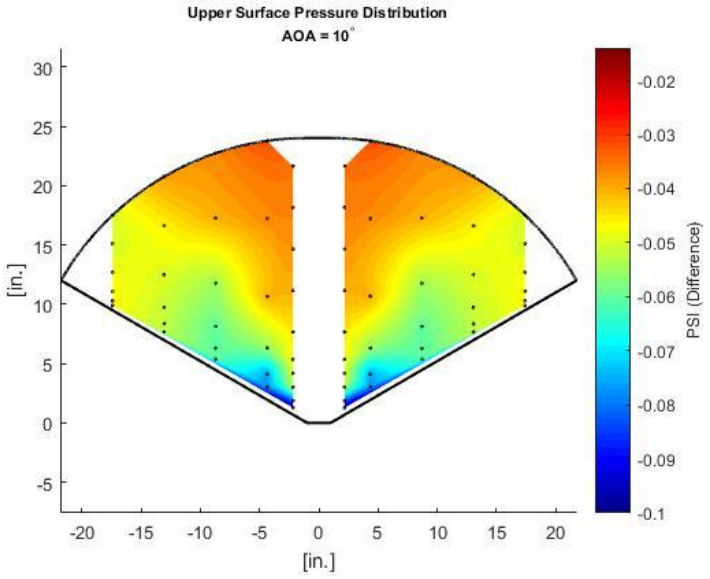

Figure 18: Upper Surface Pressure Distribution | 30-Degree Model | $\alpha = 10°$

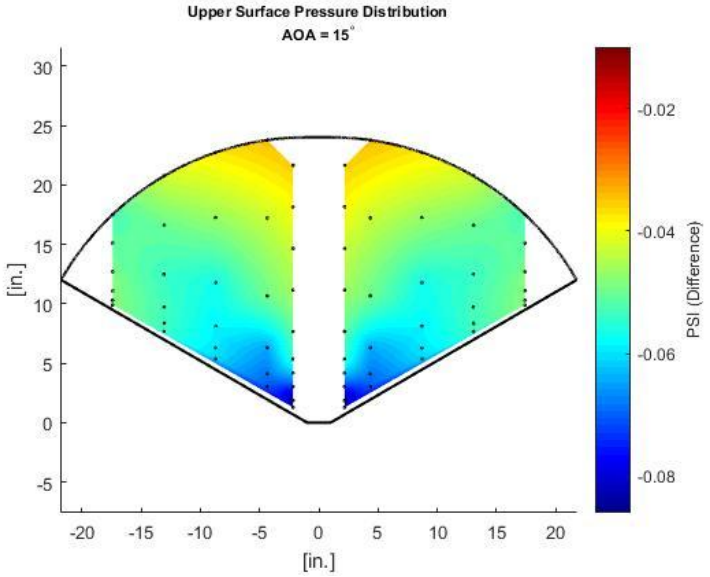

Figure 19: Upper Surface Pressure Distribution | 30-Degree Model | $\alpha = 15°$

Figure 16 through Figure 19 show the progression of the pressure distribution on the upper surface of the 30-degree model through the range of AOA. Figure 33 through Figure 48 in the Appendix show the pressure distributions on the upper and lower surface for both runs at each AOA. It is apparent that there is a low pressure region forming near the leading edge root as the angle of attack is increased. Therefore, a good region to investigate increasing wing structure would be around the quarter chord line. Looking at the difference between the lower and upper surface (see Appendix), the trailing edge of the wing also sees

a large pressure difference. This area should also be reinforced to minimize billow on the flexible plastic wing surface.

4.3 Test Results - 60-Degree Model

The results for the 60-degree model were expected to be drastically different than the 30-degree model. Since this model is highly swept, it is expected that a leading edge vortex will form according to Anderson.[7] This vortex is created because the pressure on the bottom surface of the wing at some positive angle of attack is higher than the pressure on the top surface. The flow on the bottom surface in the vicinity of the leading edge curls around the leading edge from bottom to top. Since the leading edge is moderately sharp, inviscid flow theory predicts an infinite velocity at the corner that nature copes with via separation. The separated flow curls into a vortex that re-attaches to the wing near the leading edge. This vortex creates a low pressure region that starts at the leading edge root and emanates back toward the trailing edge. An example of this vortex system is shown below in Figure 20.

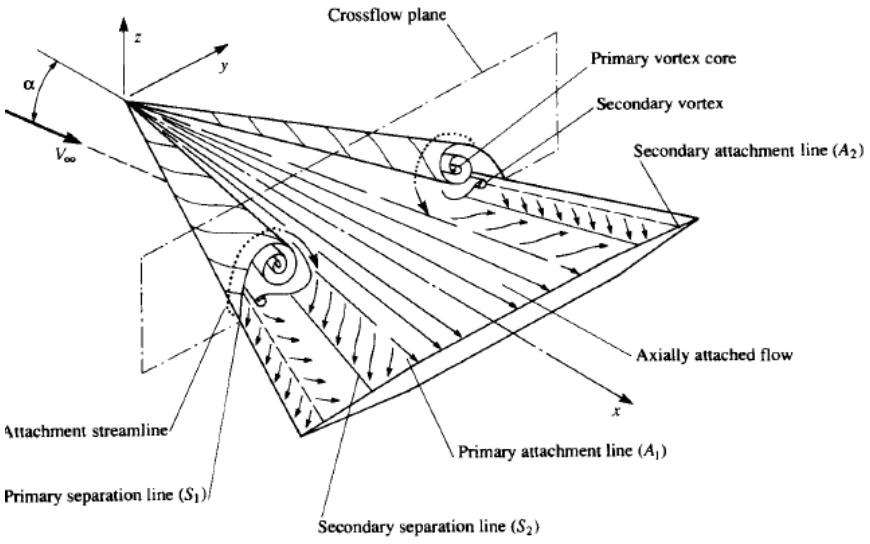

Figure 20: Flow Field Over Delta Wing [7]

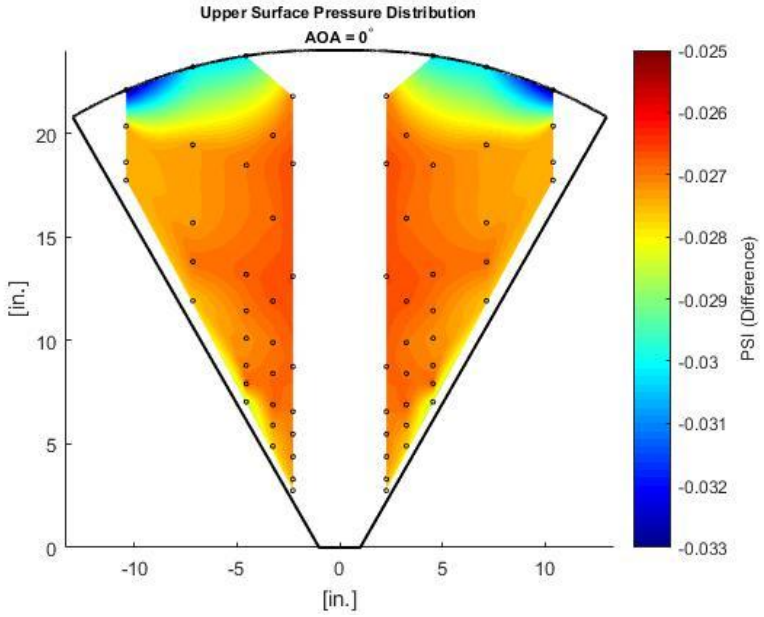

Figure 21: Upper Surface Pressure Distribution | 60-Degree Model | α = 0°

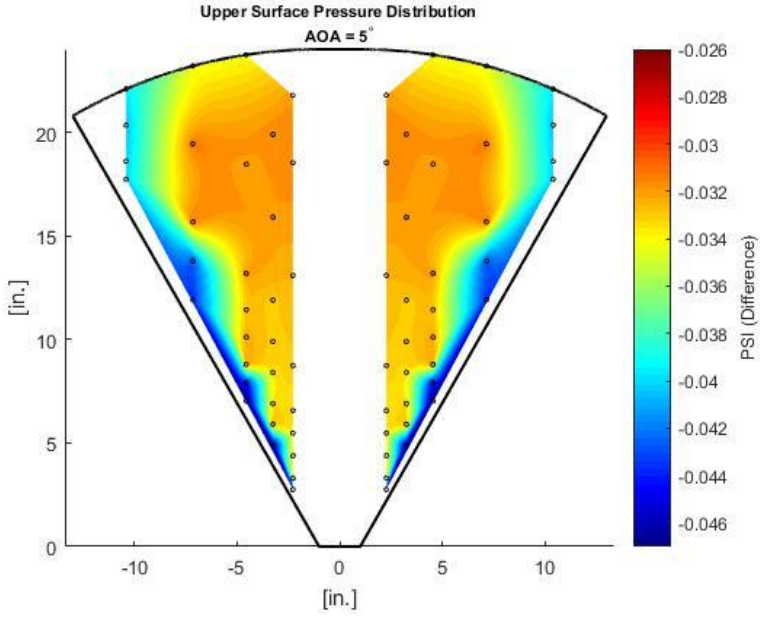

Figure 22: Upper Surface Pressure Distribution | 60-Degree Model | α = 5°

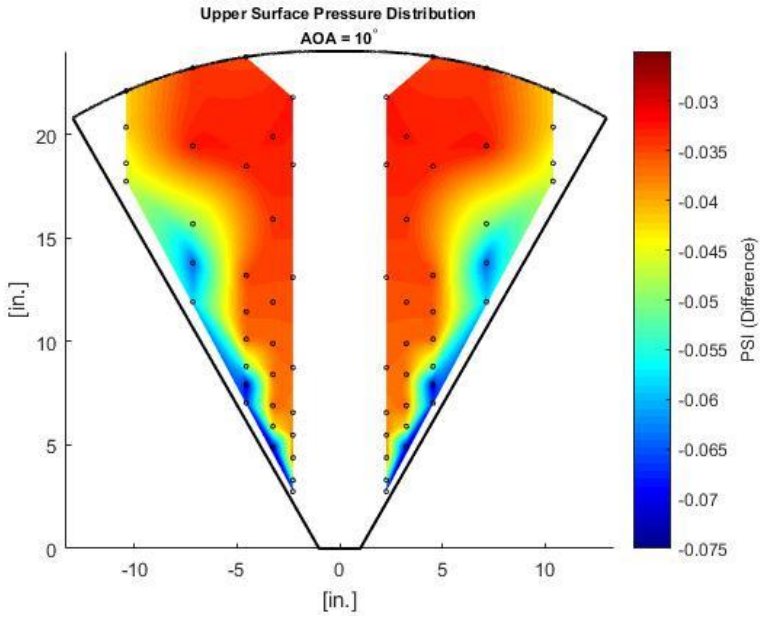

Figure 23: Upper Surface Pressure Distribution | 60-Degree Model | α = 10°

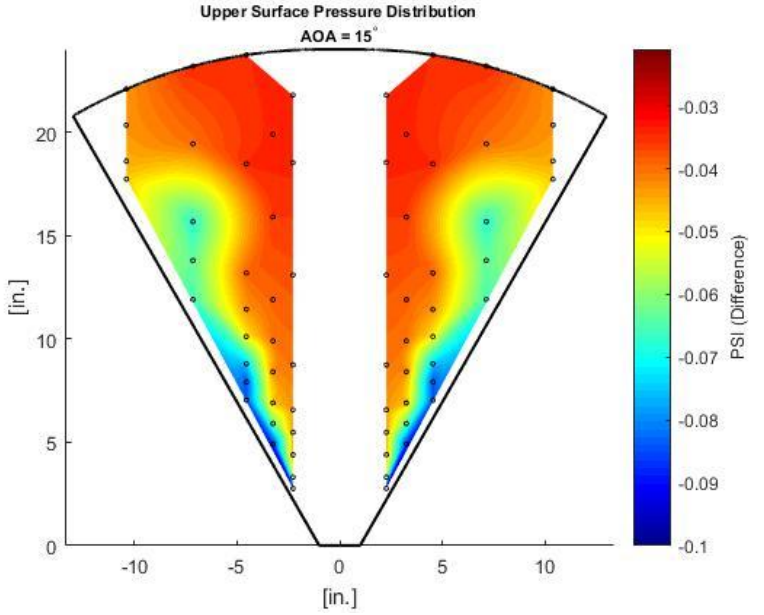

Figure 24: Upper Surface Pressure Distribution | 60-Degree Model | α = 15°

Figure 21 through Figure 24 show the progression of the pressure distribution on the upper surface of the 60-degree model through the range of AOA. At 5 degrees it is clear that the leading edge vortex system has formed. When the model is pitched to 10 degrees AOA the vortex system has strengthened toward the root, but it weakens in strength around 75% span. The same pattern occurs at 15

degrees AOA. This "weakening" is known as vortex breakdown, and is a phenomenon depicted by Anderson.

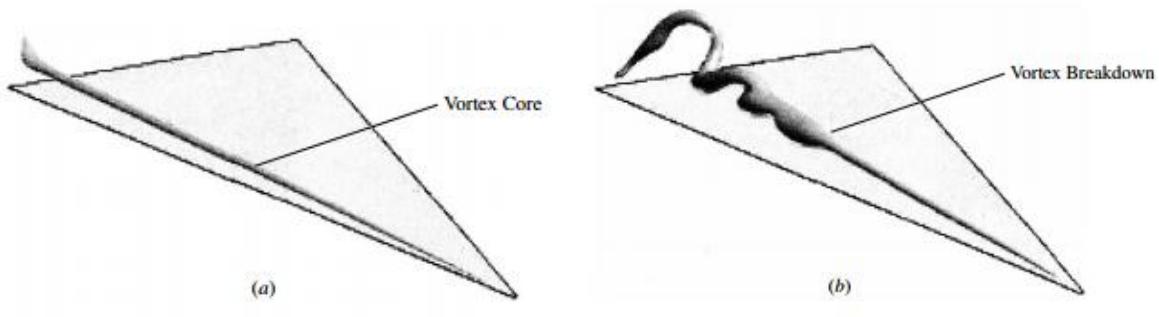

Figure 25: a) 60° Delta Wing at α = 5° b) 60° Delta Wing at α = 15° [7]

At 5 degrees AOA, the vortex is tightly attached to the wing for the full length of the wing. However, at higher angles of attack the vortex breaks down. The results in Figure 24 clearly show a tight vortex at the root that breaks down around 60% span, as depicted in Figure 25b.

The results of the 60-degree model show that the largest pressure difference will be around quarter chord where the leading edge vortex has formed. Figure 49 through Figure 64 in the Appendix give the full results for the upper and lower surfaces of the 60-degree model for both runs at all angles of attack. The trailing edge should again be reinforced to minimize billow due to the large pressure difference between upper and lower surfaces.

Chapter 5: FEM Analysis of Wing Structure Design

5.1 Wing Structure Designs

An important aspect of this research project is to understand how wing structural components behave under loading. This is critical for quantifying wing deflection and ensuring wing structure survivability. In previous research, Whitfield investigated the wing loading distribution on a 30-degree model with seven ribs. Static pressure ports were installed on the upper and lower surface of each rib and pressure measurements were taken along the wing span at three chord-wise locations to quantify the wing loading distributions with the installed structural components.[3]

The model was used to measure the wing loading distribution at 0.25, 0.50, and 0.75 cord-wise locations. The results of this test at 10 and 15 degrees AOA are shown below.

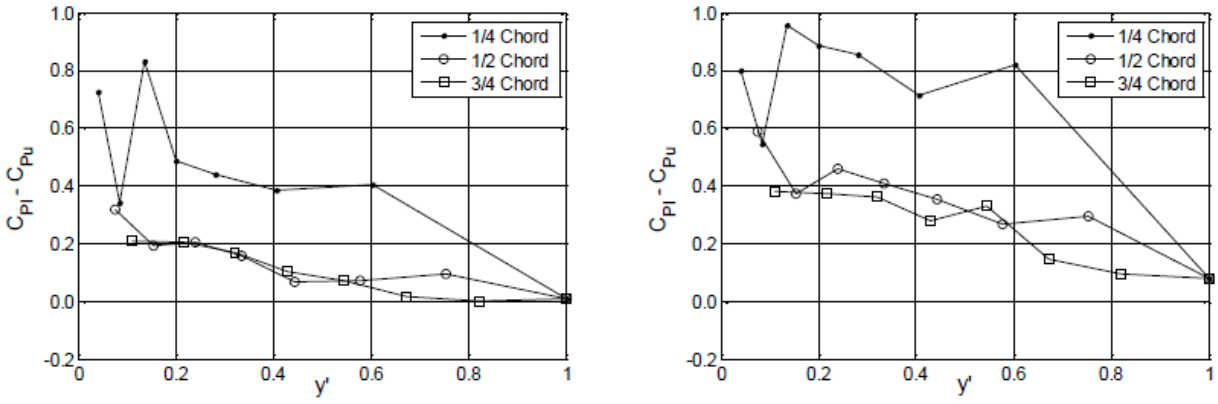

Figure 26: Pressure Difference Distribution | α = 10° Left, α = 15° Right [3]

This data was used for the FEM analysis because the results in Chapter 4 had not been acquired yet. As mentioned in Section 1.3, the sweep angle is 30 degrees because this model is expected to see the largest stresses.

The root chord for the models analyzed was set at 10 feet. This was chosen because a 10-foot model is the first step of prototype development, and understanding the loading on this model is important to ensure the wing structure is not compromised. The structures analyzed used 2.5" OD, 2.25" ID commercially available carbon fiber tube for the wing structure. Top views of the left half wing designs are shown below in Figure 27.

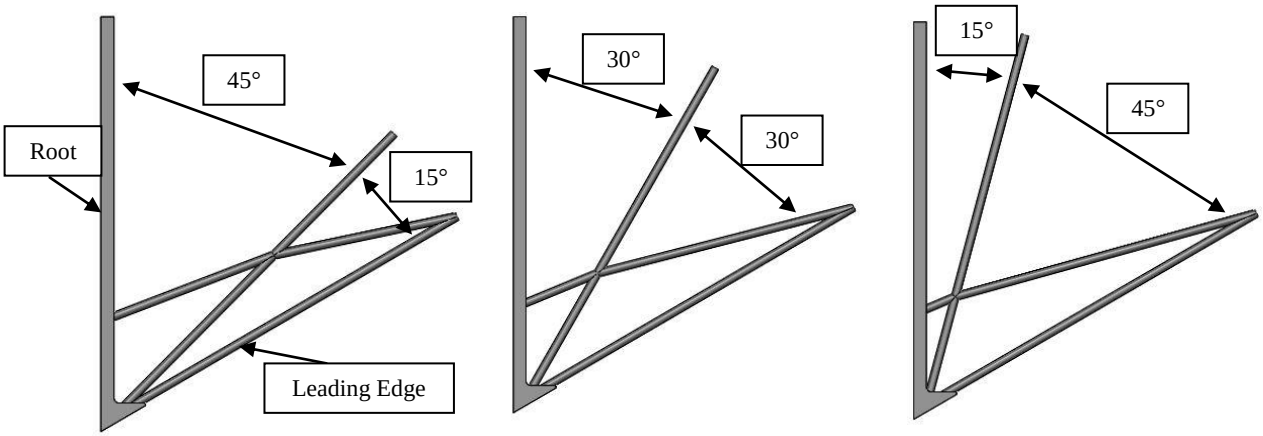

Figure 27: Top View of 10-Foot Models Under Investigation

The models use a spar that runs along the quarter chord of the UAV to the tip of the wing. Another spar runs from the leading edge root to the trailing edge of the wing. The angle that this spar runs with respect to the leading edge spar ranges from 15 to 45 degrees.

5.2 FEM Setup

SolidWorks FEM was used for this analysis. The mesh used tetrahedral elements with a maximum edge length of 0.42 inches and minimum edge length of 0.021 inches. The total number of elements for each model was around 230,000 elements. The material properties used were for high modulus carbon fiber fabric, available from the manufacturer. These properties are listed below in Table 6. It should be noted that this structural analysis uses the assumption that carbon fiber is an isotropic material. This is not the case in reality as carbon fiber is an anisotropic material. However, for the purposes of this analysis, and using the assumption that the laminate layup is the same in all directions, the results give a close approximation to the actual deflections and stresses expected.

Table 6: Material Properties of High Modulus Carbon Fiber

Material Properties		
Young's Modulus (GPa)	Poisson's Ratio	Ultimate Stress (Mpa)
85	0.1	350

The FEM analysis used symmetry about the center of the wing to reduce computational cost. The face used as the plane of symmetry was clamped using a fixed boundary condition (all degrees of freedom on the face were set equal to zero). Point loads were then placed at the locations where pressure was measured in Figure 26. These point loads were determined from the difference in Cp given by Whitfield. It should be noted that only the port locations that lay on the new structure were used. The magnitude of these point loads was calculated from the following equations where C_n is the local normal force coefficient, C_P is the pressure coefficient, N is the local normal force, ρ is the density at deployment altitude (62,000 ft)[2], V is the flight velocity (150 ft/s)[2], and MAC is the mean aerodynamic chord.[4]

Equation 3: Local Normal Force Coefficient

$$C_n = \Delta C_P$$

Equation 4: Local Normal Force

$$N = \frac{1}{2}\rho V^2 C_n \, MAC$$

The boundary conditions and point loads for the three rib model are shown below in Figure 28 and Figure 65 through Figure 67 of the appendix for the new structural layouts.

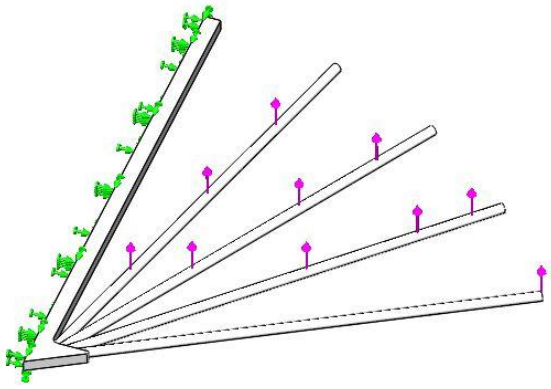

Figure 28: Boundary Conditions Applied to Three Rib Model

5.3 Results and Discussion

The displacement for the three rib, the 45°/15°, the 30°/30°, and the 15°/45° models using the pressures at 15 degrees AOA are shown below in Figure 29 through Figure 32. The displacement at 10 degrees AOA and the von Mises stress at both 10 and 15 degrees AOA for each model are shown in Figure 68 through Figure 76 in the appendix.

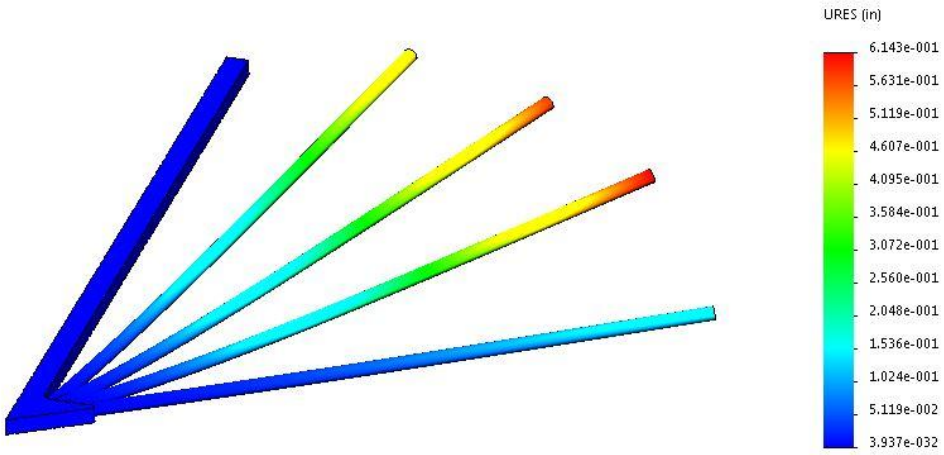

Figure 29: Displacement [in.] | Three Rib Model | 15° AOA

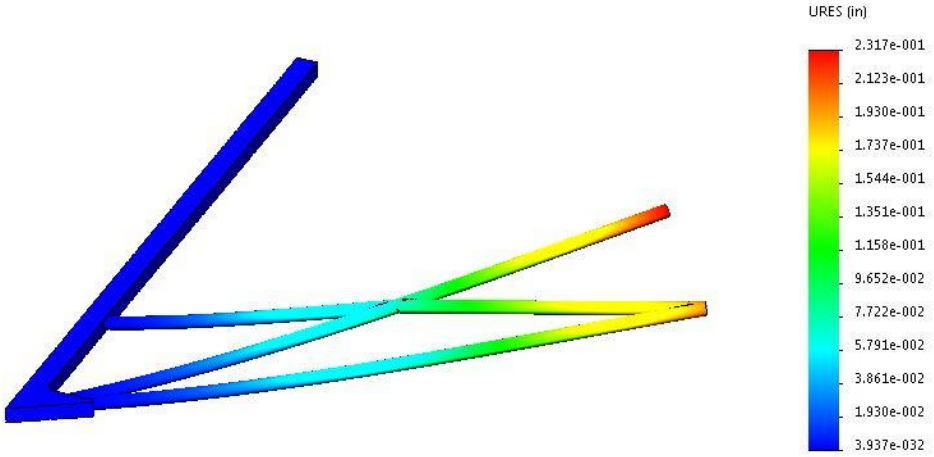

Figure 30: Displacement [in.] | 45/15 Model | 15° AOA

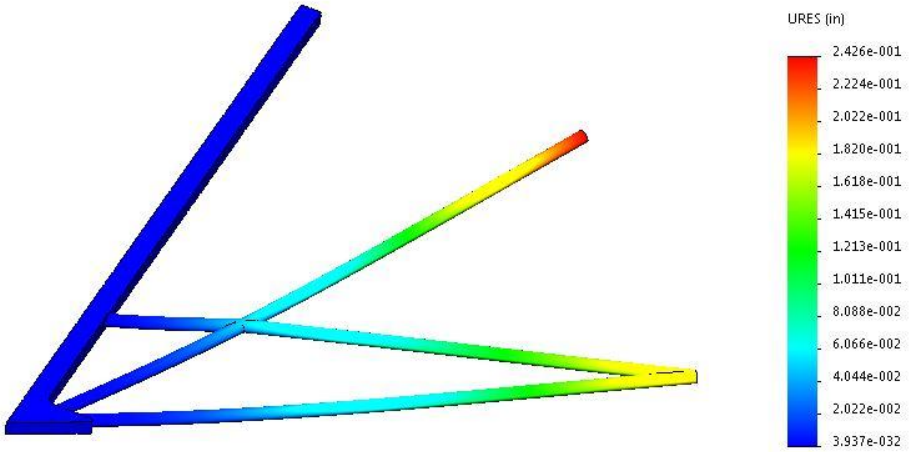

Figure 31: Displacement [in.] | 30/30 Model | 15° AOA

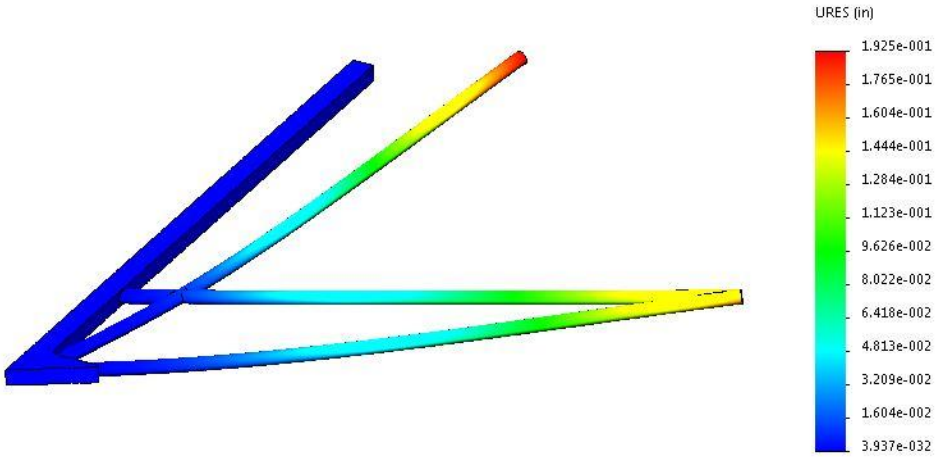

Figure 32: Displacement [in.] | 15/45 Model | 15° AOA

A few key results come out of this analysis. The maximum deflection occurs at the tip of the central rib for each model. This means that the wing would have a slight billow, possibly decreasing L/D. Also, the 30/30 model has the highest deflection out of all of the designs (excluding the three rib model). This is interesting because the 45/15 model was expected to have the highest deflections due to the proximity of the structure to the higher aerodynamic loadings occurring along the quarter chord line.

This analysis is by no means comprehensive. In the future it should be expanded to a higher fidelity software such as ANSYS APDL. This software has the ability to analyze anisotropic materials. Also, the results from Section 4.2 and 4.3 should be incorporated into the model because the pressure distribution is more refined. Finally, the entire assembly of the wing (wing skin and structural ribs) should

be investigated using higher fidelity FEM analysis. SolidWorks FEM only allows the analysis of single parts; however, ANSYS APDL allows for analysis of entire assemblies. This has the ability to overlay the pressure distribution obtained from this research to the wing skin, model the contacts between the wing skin and the wing structure, and give a more accurate representation of the expected stresses and deflections. The downside to the analysis described is a drastic increase in computational time and problem formulation/setup.

Chapter 6: Conclusions and Future Work

The goal of this research project was to experimentally determine the pressure distribution on delta-type wings for two UAV configurations with different leading edge sweep angles. The models needed to be investigated at multiple angles of attack, necessitating the development of a mounting system with the capability of quickly adjusting to various angles of attack. This mount also had to hold the models centered in the wind tunnel to avoid interference with the walls of the tunnel, accommodate multiple wind tunnel models, and maintain lab equipment flexibility for future use. The sting mount was machined using a lathe and a traditional three-axis mill. Stainless steel rod was used for the sting, and aluminum plate was used for the angle of attack adjustment plate.

The models were fabricated from 1/8" stainless steel plate and cut using a waterjet. Slots were machined in the plate and two stainless steel rods for alignment of the leading edge spars. The rods were then TIG welded to the leading edge of the plate. The welds were sanded flush and the models were polished. 1/16" stainless steel tubing elbows were fabricated and glued in the pressure tap holes with J.B. Weld. Tygon tubes were then attached to the free end of the stainless steel tubing and connected to the pressure transducers. These models were mounted to a fuselage spike that attached directly to the sting. The models were investigated at the full-scale Reynolds Number of 500,000 – varying the angle of attack from 0 to 15 degrees in five degree increments. Pressure transducers were used to measure pressure at 68 locations on each model. The pressure distribution results compared well with theory for delta wings in low speed flow – especially for predicted leading-edge vortex breakdown on the 60-degree model at 15 degrees AOA. The pressure distributions can now be used to lay out the structural design of flexible delta-type wings.

FEM analysis was also utilized to understand how different wing structure configurations behave in multiple flight conditions. SolidWorks FEM was chosen due to its simplicity and ease of use. The

structures were built of high modulus carbon fiber fabric and approximated as isotropic materials. The midpoint of the wing was clamped with an all degrees of freedom equal to zero boundary condition. Point loads were then applied on the structure as provided by [3]. Each model showed that the highest stress occurred at the root of the quarter chord spar. Also, the 30/30 model surprisingly showed the highest stress concentration out of all three models. These results can now be used by the UAV designer to narrow down the selection for future wing structure designs.

Now that the pressure distributions are known, more wing structure designs should be developed. These new designs should also be analyzed in higher fidelity FEM software utilizing the pressure distributions collected in this research. Future FEM analyses should use anisotropic material properties at minimum. If possible, the entire wing assembly should be analyzed in FEM software using the pressure distributions obtained in this research for an accurate representation of stress concentrations and deflections. This would lead to vehicle designs that have better aerodynamic performance at a lower structural weight, increasing the performance and endurance of the UAV.

References

[1] Pearson, J., U.S. Patent 9,272,783 B2, 2016.

[2] Whitfield, C.A., High-altitude Morphing UAV Conceptual Design, Whitfield Aerospace LLC, 2009.

[3] Whitfield, C. Aerodynamic Performance Characteristics of Flexible Polyimide Film Delta-type Wings.

[4] Barlow, J. B., William, R. H., and Pope, A. *Low-Speed Wind Tunnel Testing.* 3rd Ed. Wiley India Pvt. Ltd.

[5] TSI Incorporated. *Model 8350 VELOCICALC Air Velocity Meter*. July, 1989.

[6] Allenstein, Jacob T. *An Investigation in Gold-Plating Scaled Turbofan Engine Simulators through Means of Aerodynamic and Load Cell Thrust Measurements with Comparison to Full-Scale Engine Results.* Master of Science Thesis. The Ohio State University, 2013.

[7] Anderson Jr., J. D. (2010). *Fundamentals of Aerodynamics*. 5th Ed. Boston: McGraw-Hill.

Appendix

Table 7: Wind Tunnel Test Parameters

	MAC (ft)	Run	AOA (deg)	Standard Velocity (ft/s)	Actual Velocity (ft/s)	Ambient Temperature (°F)	Ambient Pressure (PSIA)	Density (slugs/ft^3)	Dynamic Viscosity (slug/ ft s)	Reynolds Number
Λ = 30°	1.47	1	1.20	57.75	57.97	74.87	14.779	0.0023201	3.705E-07	533,586
		2	1.20	55.23	55.26	73.22	14.779	0.0023273	3.696E-07	511,475
		1	5.80	56.38	56.47	73.78	14.779	0.0023249	3.699E-07	521,702
		2	5.80	56.15	56.24	73.68	14.779	0.0023253	3.699E-07	519,695
		1	11.75	56.10	56.18	73.60	14.779	0.0023256	3.698E-07	519,293
		2	11.75	56.75	56.87	74.00	14.779	0.0023239	3.701E-07	525,006
		1	15.80	57.08	57.18	73.79	14.779	0.0023248	3.699E-07	528,250
		2	15.80	56.10	56.25	74.32	14.779	0.0023225	3.702E-07	518,752
Λ = 60°	1.36	1	0.59	53.33	52.89	58.37	14.497	0.0023483	3.616E-07	467,113
		2	0.59	53.02	52.52	57.78	14.497	0.0023510	3.613E-07	464,751
		1	5.65	53.43	52.85	56.97	14.497	0.0023547	3.609E-07	468,975
		2	5.65	53.38	52.76	56.66	14.497	0.0023561	3.607E-07	506,591
		1	11.63	52.55	51.94	56.63	14.497	0.0023562	3.607E-07	461,459
		2	11.63	52.23	51.56	55.92	14.497	0.0023595	3.603E-07	459,170
		1	15.75	53.43	52.88	57.25	14.497	0.0023534	3.610E-07	468,778
		2	15.75	51.83	51.26	56.87	14.497	0.0023552	3.608E-07	455,001

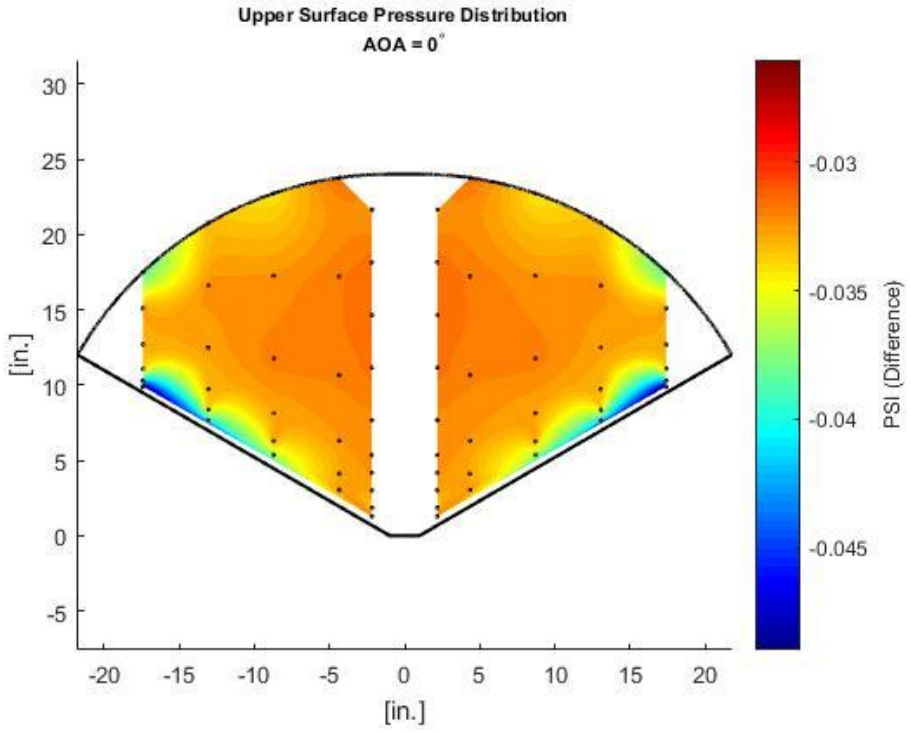

Figure 33: Λ = 30° | Upper Surface | α = 0° | Run 1

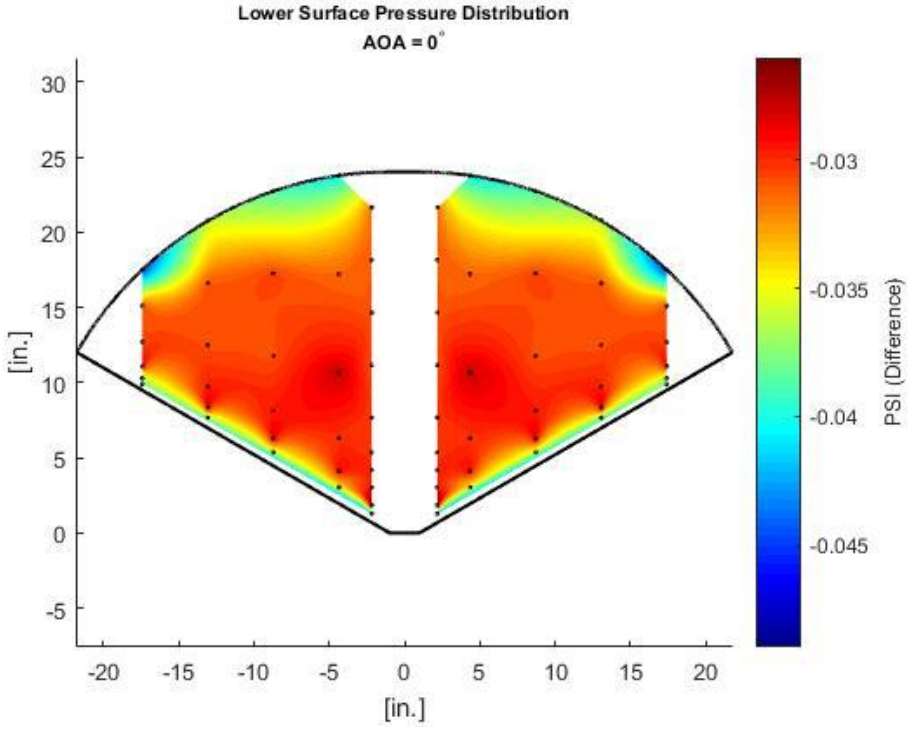

Figure 34: Λ = 30° | Lower Surface | α = 0° | Run 1

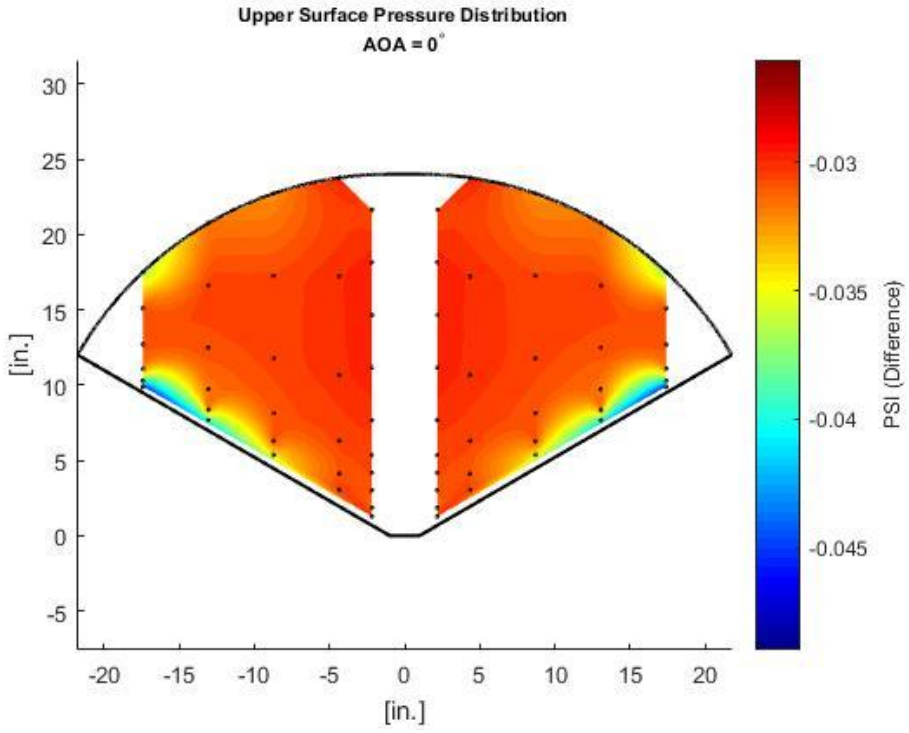

Figure 35: Λ = 30° | Upper Surface | α = 0° | Run 2

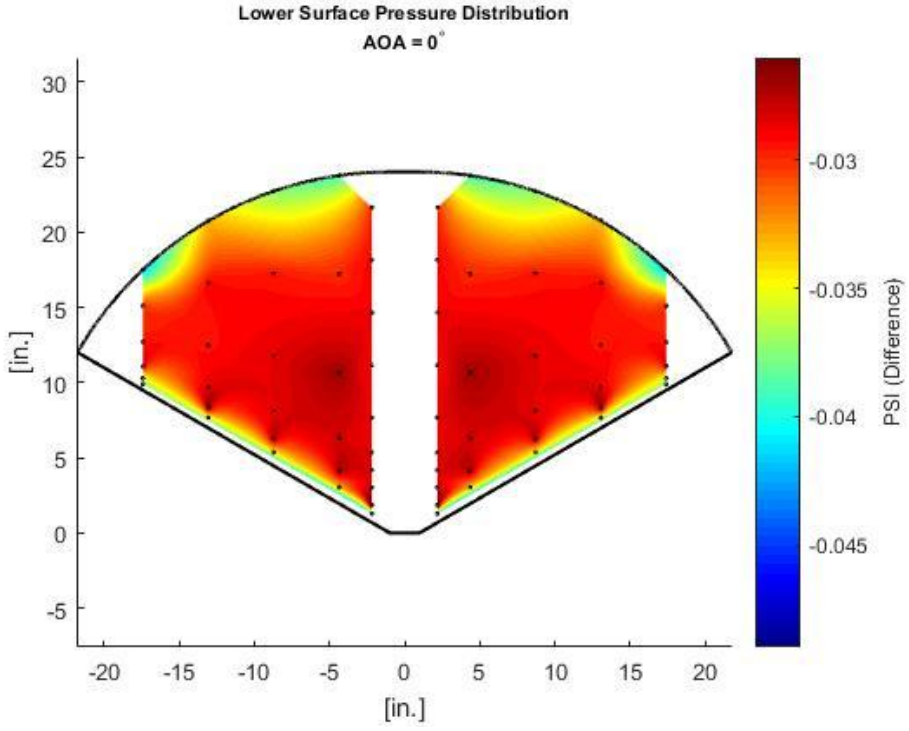

Figure 36: Λ = 30° | Lower Surface | α = 0° | Run 1

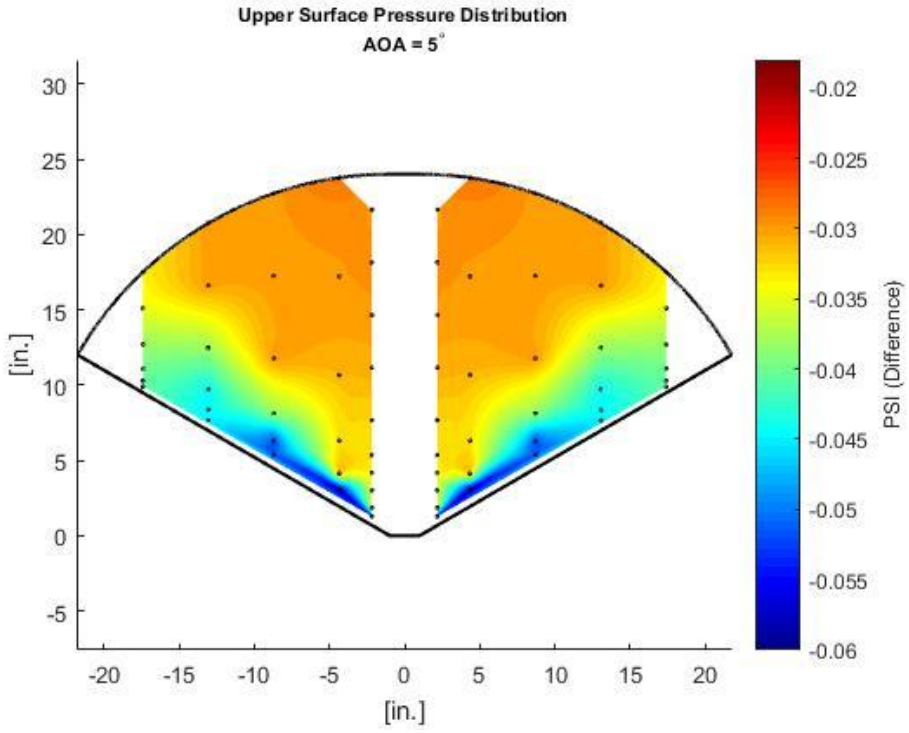

Figure 37: Λ = 30° | Upper Surface | α = 5° | Run 1

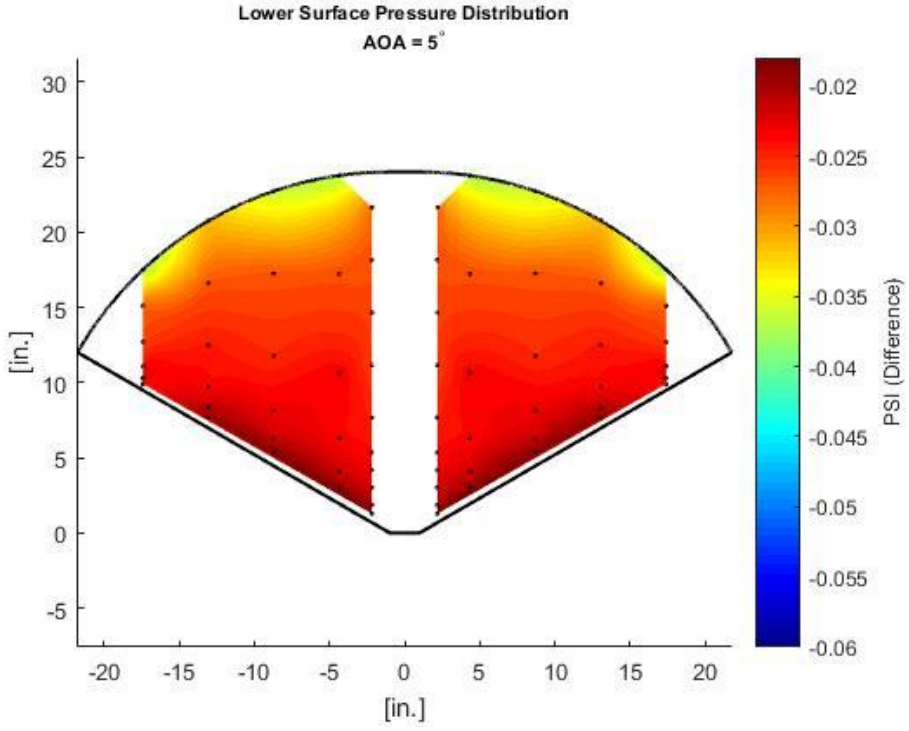

Figure 38: Λ = 30° | Lower Surface | α = 5° | Run 1

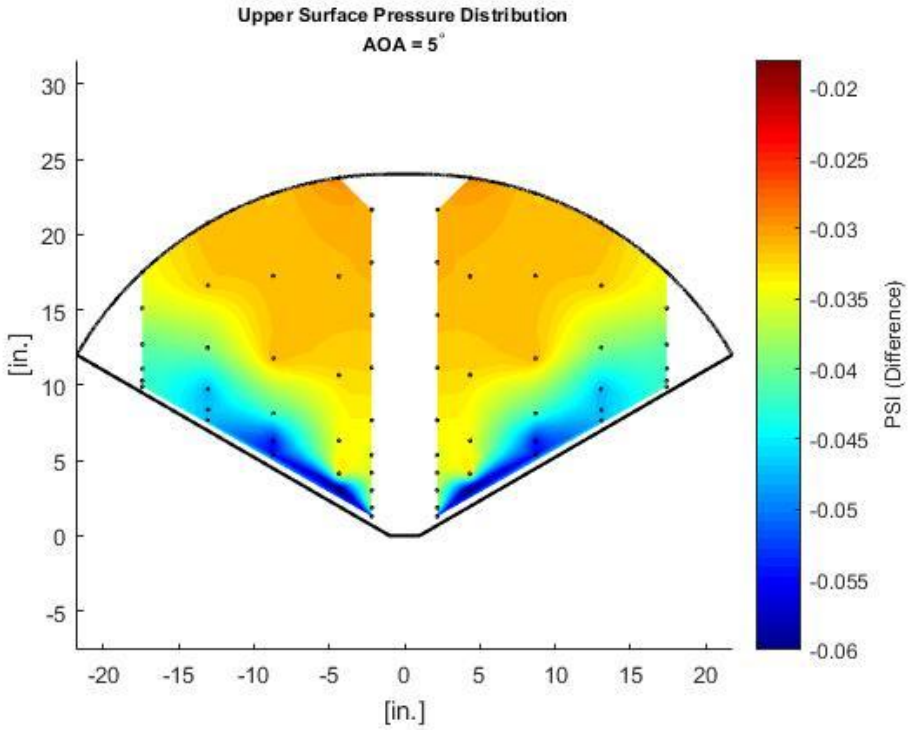

Figure 39: Λ = 30° | Upper Surface | α = 5° | Run 2

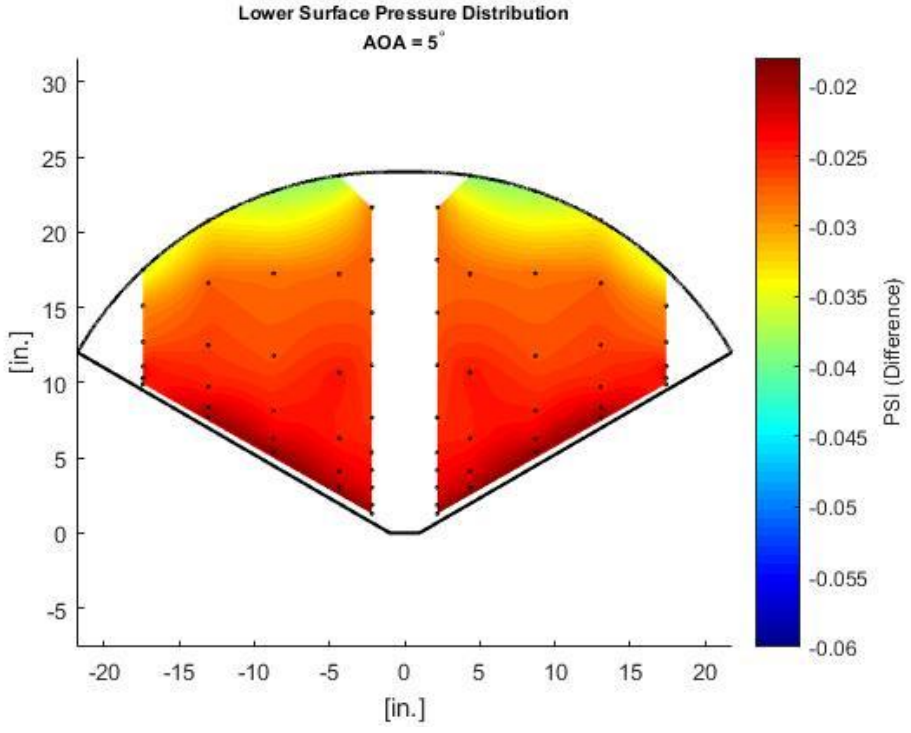

Figure 40: Λ = 30° | Lower Surface | α = 5° | Run 2

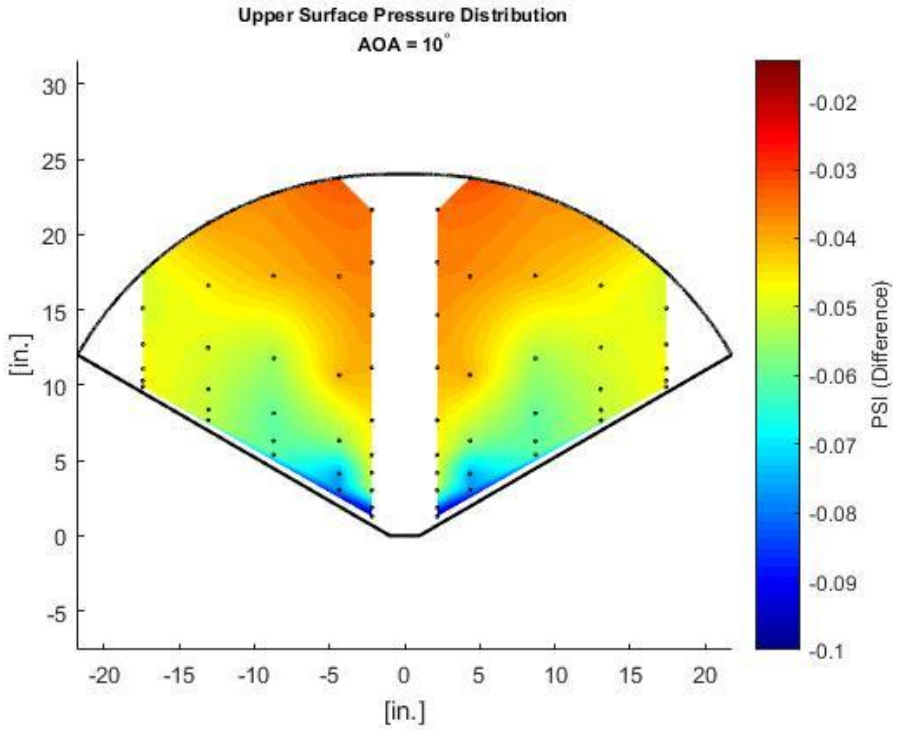

Figure 41: Λ = 30° | Upper Surface | α = 10° | Run 1

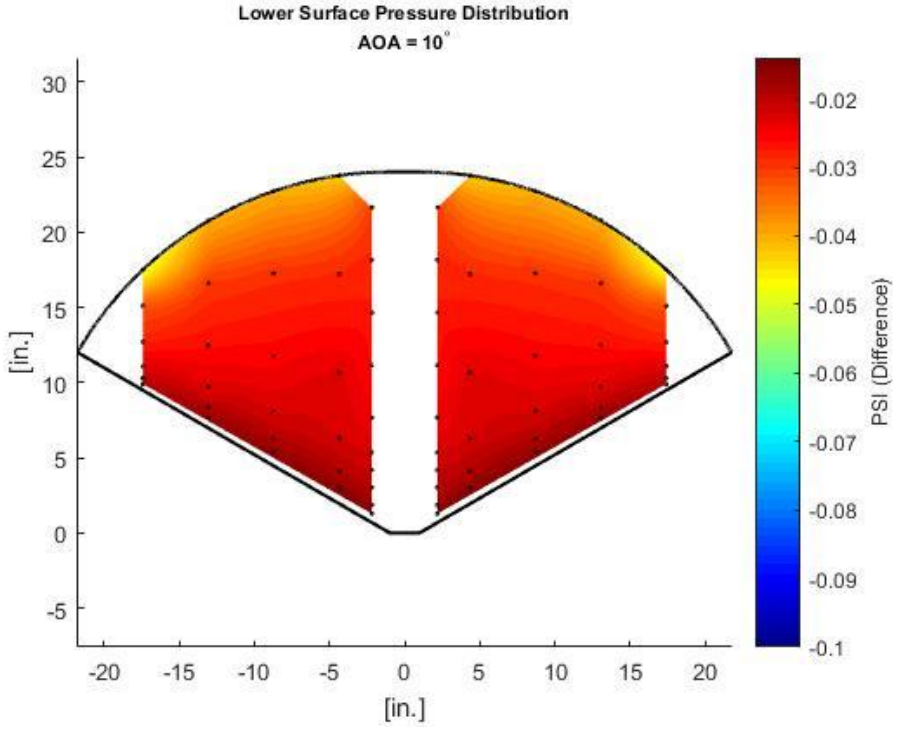

Figure 42: Λ = 30° | Lower Surface | α = 10° | Run 1

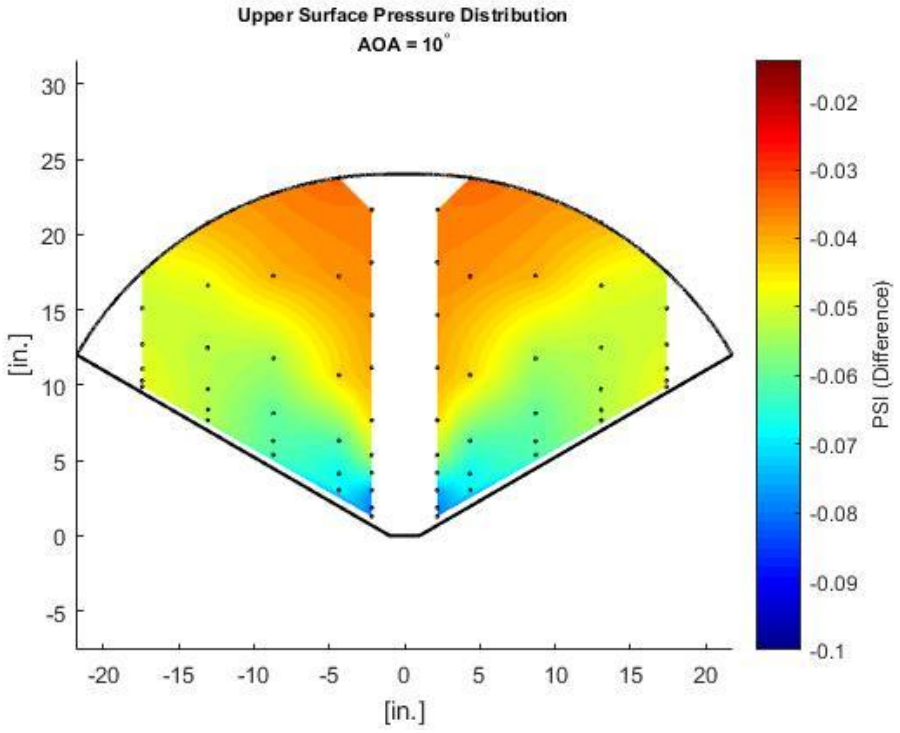

Figure 43: Λ = 30° | Upper Surface | α = 10° | Run 2

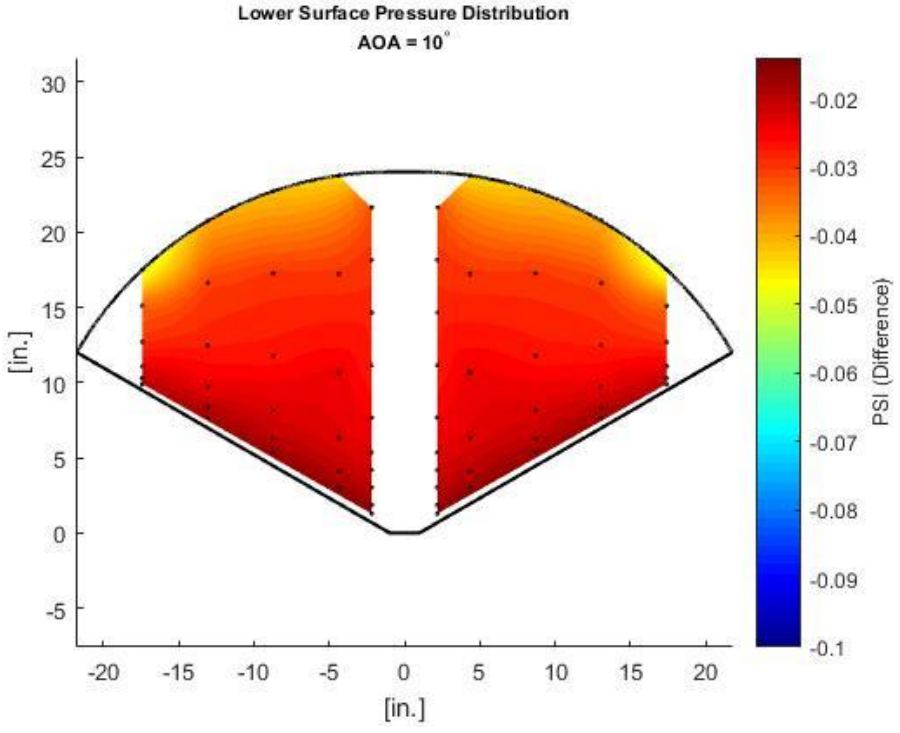

Figure 44: Λ = 30° | Lower Surface | α = 10° | Run 2

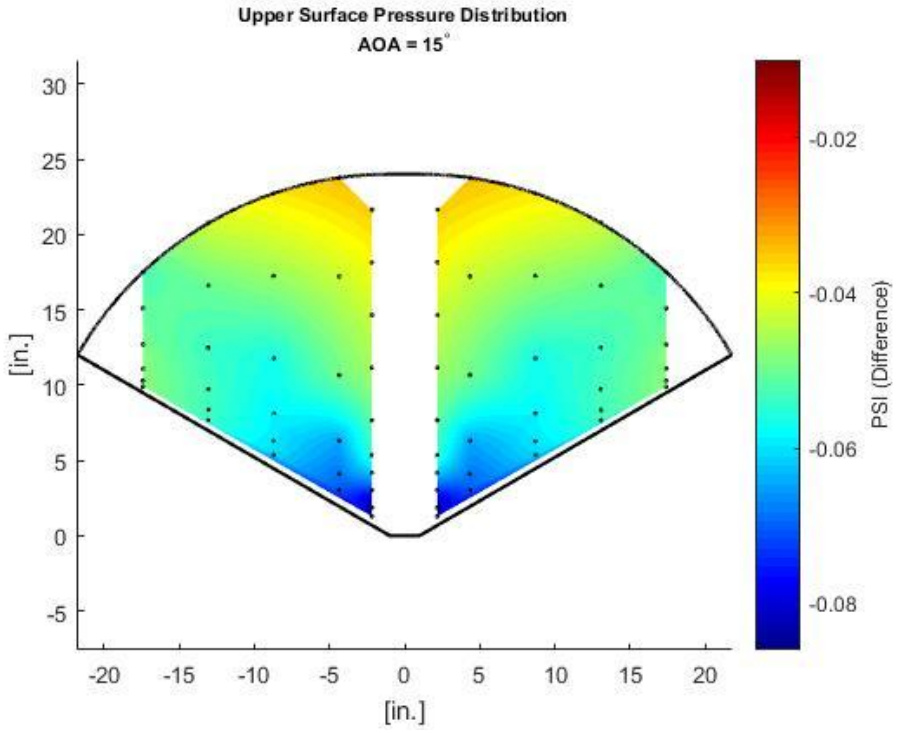

Figure 45: Λ = 30° | Upper Surface | α = 15° | Run 1

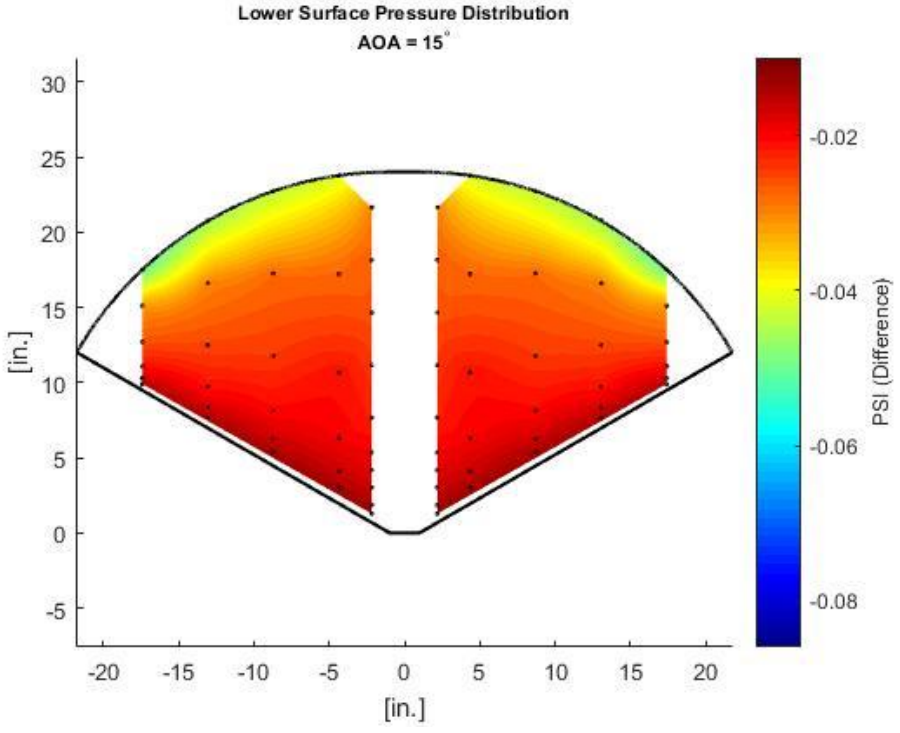

Figure 46: Λ = 30° | Lower Surface | α = 15° | Run 1

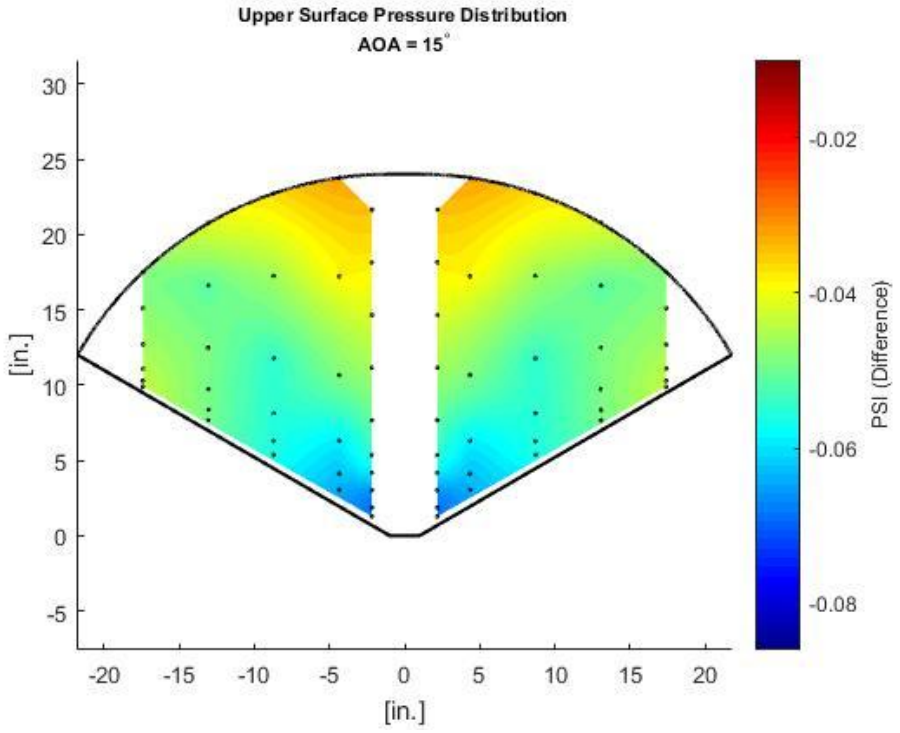

Figure 47: Λ = 30° | Upper Surface | α = 15° | Run 2

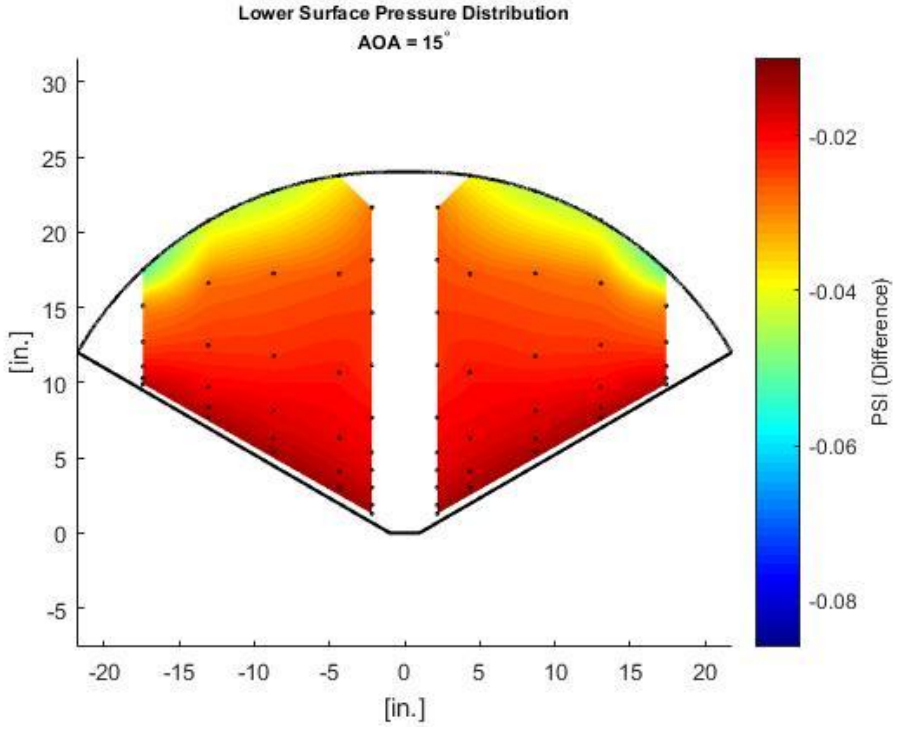

Figure 48: Λ = 30° | Lower Surface | α = 15° | Run 2

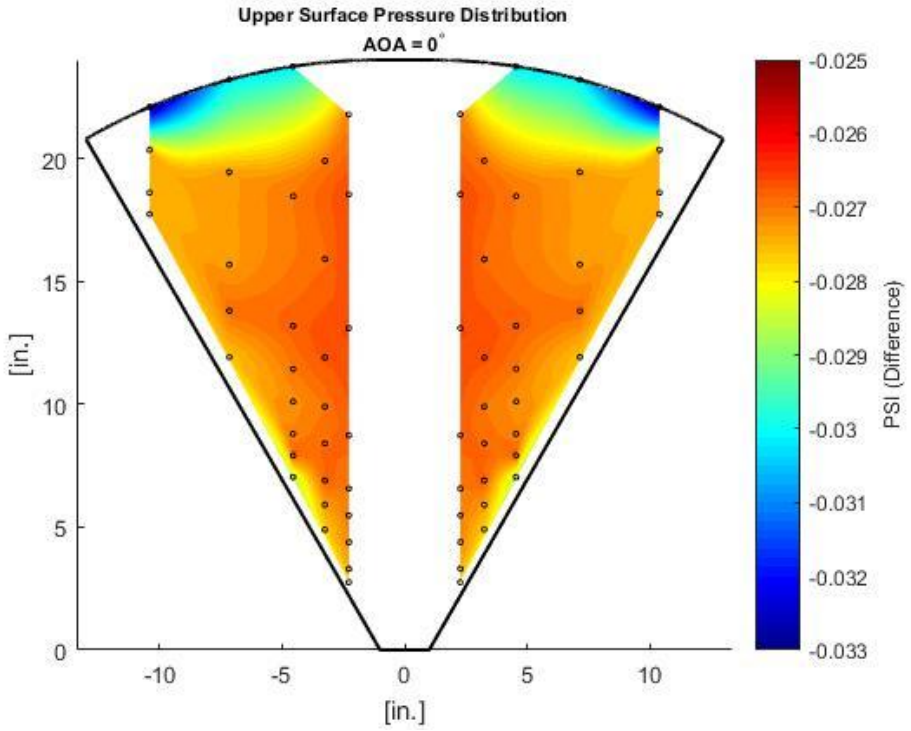

Figure 49: Λ = 60° | Upper Surface | α = 0° | Run 1

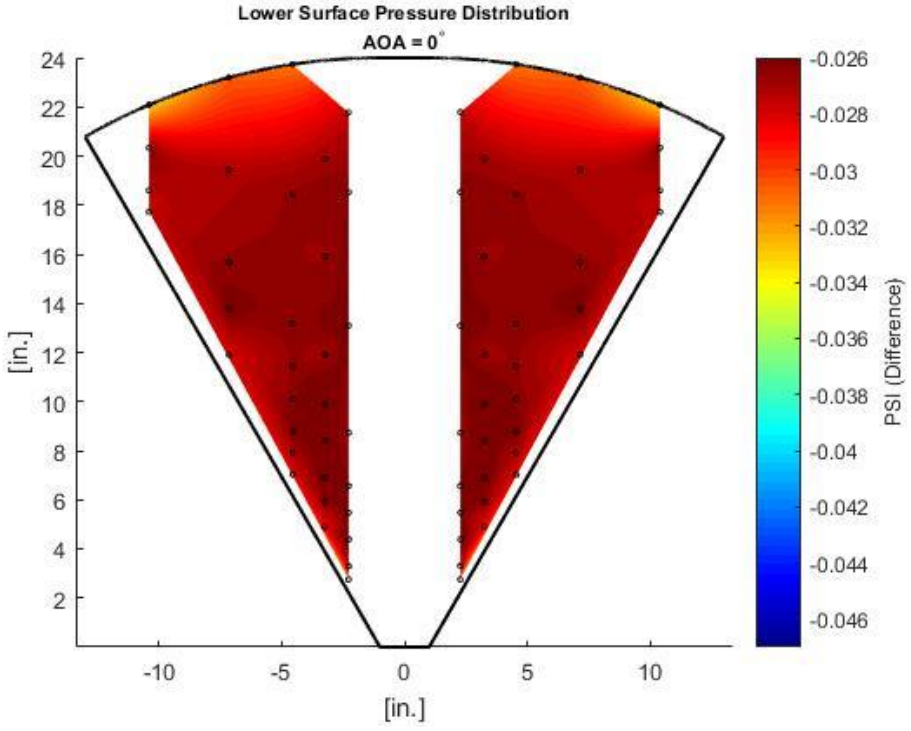

Figure 50: Λ = 60° | Lower Surface | α = 0° | Run 1

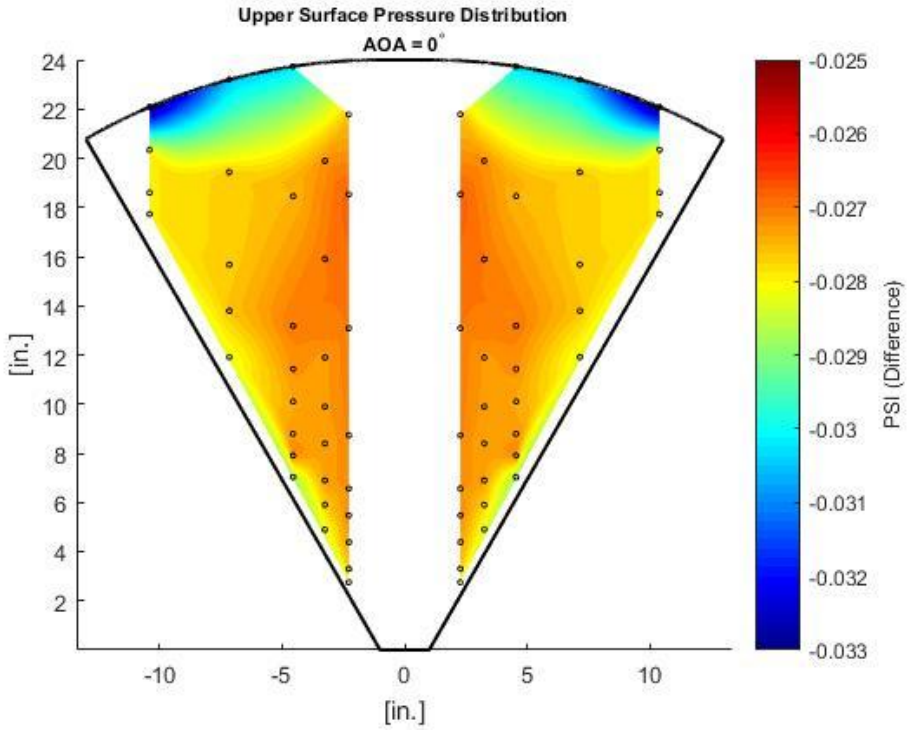

Figure 51: Λ = 60° | Upper Surface | α = 0° | Run 2

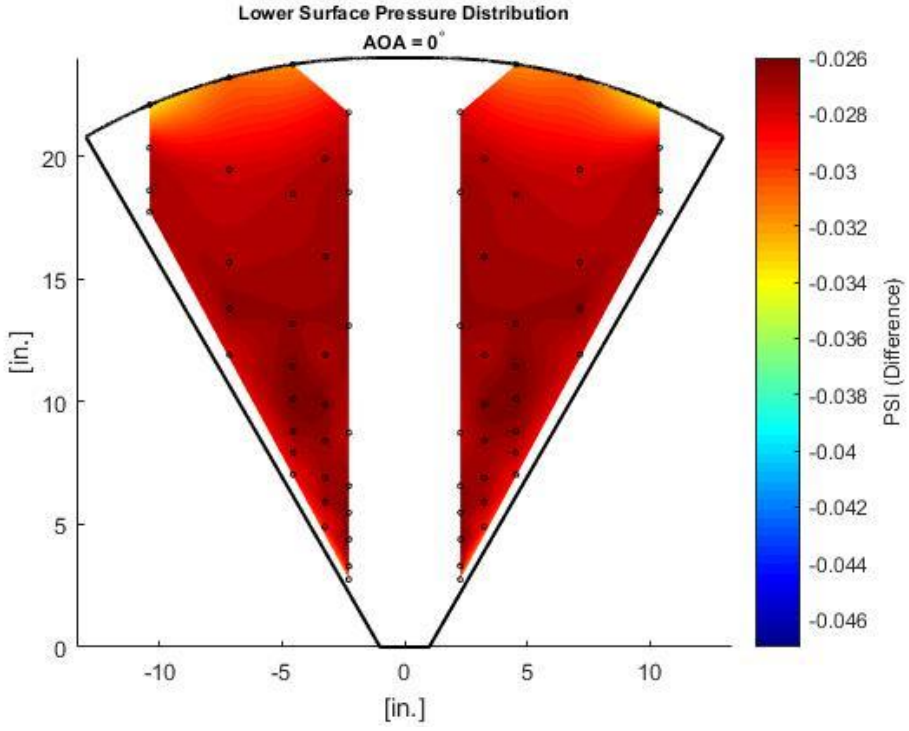

Figure 52: Λ = 60° | Lower Surface | α = 0° | Run 2

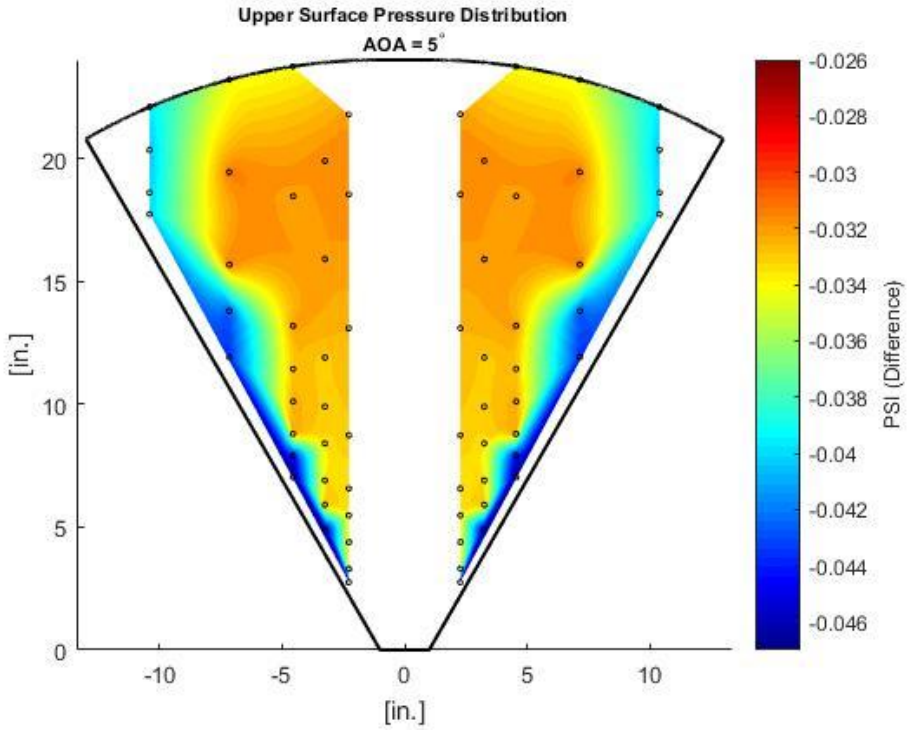

Figure 53: Λ = 60° | Upper Surface | α = 5° | Run 1

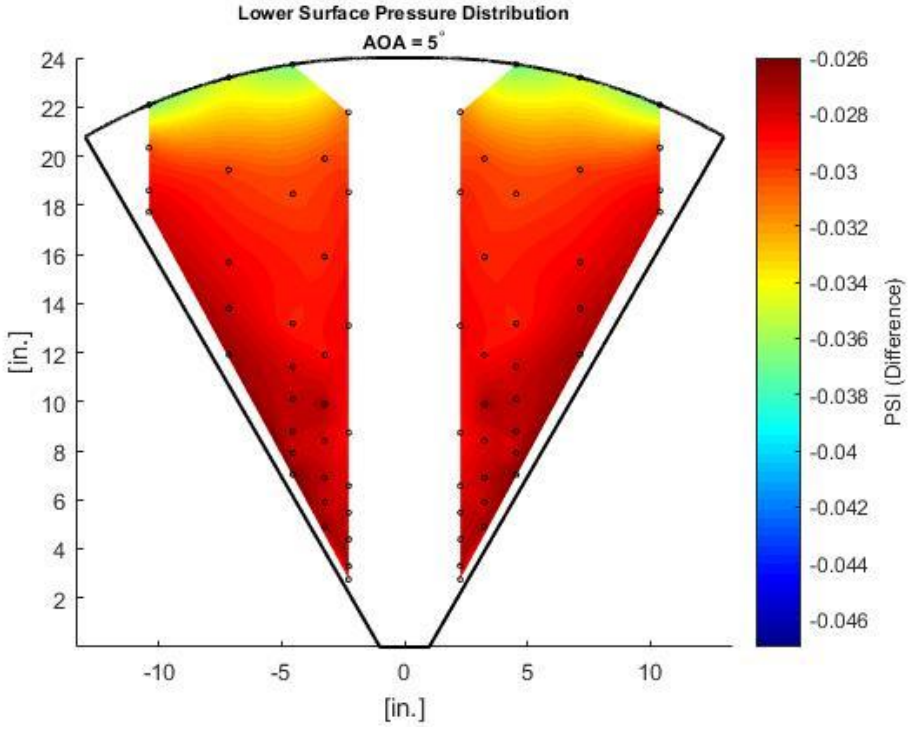

Figure 54: Λ = 60° | Lower Surface | α = 5° | Run 1

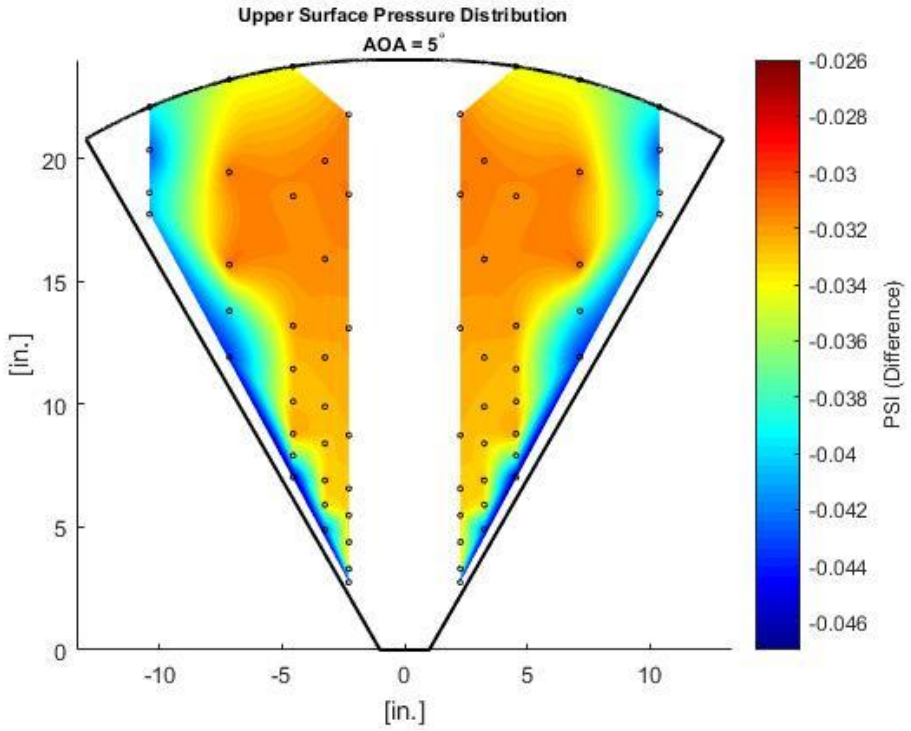

Figure 55: Λ = 60° | Upper Surface | α = 5° | Run 2

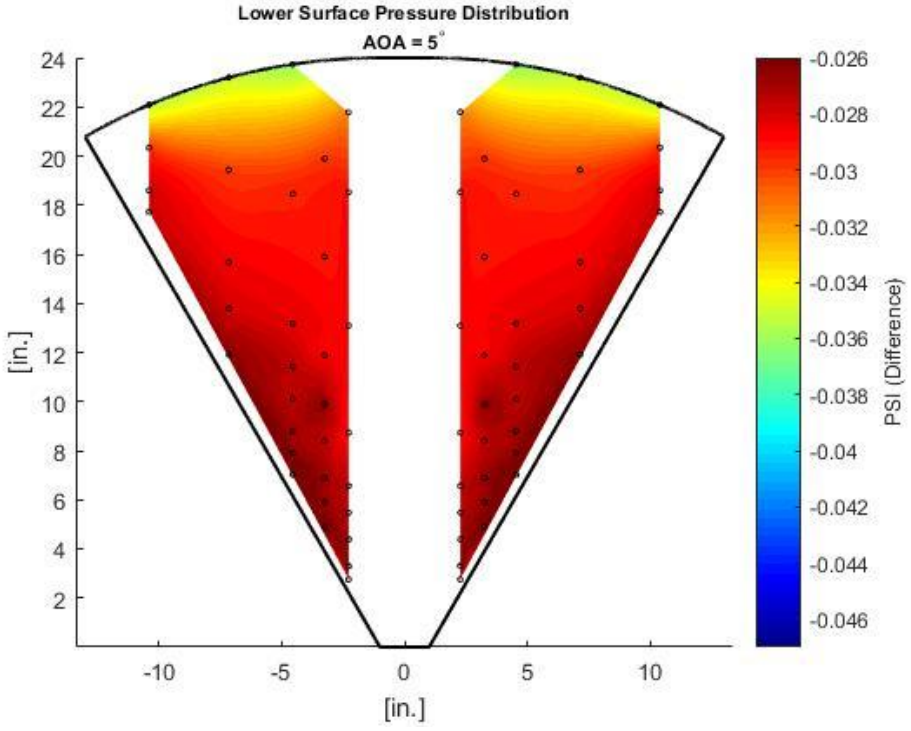

Figure 56: Λ = 60° | Lower Surface | α = 5° | Run 2

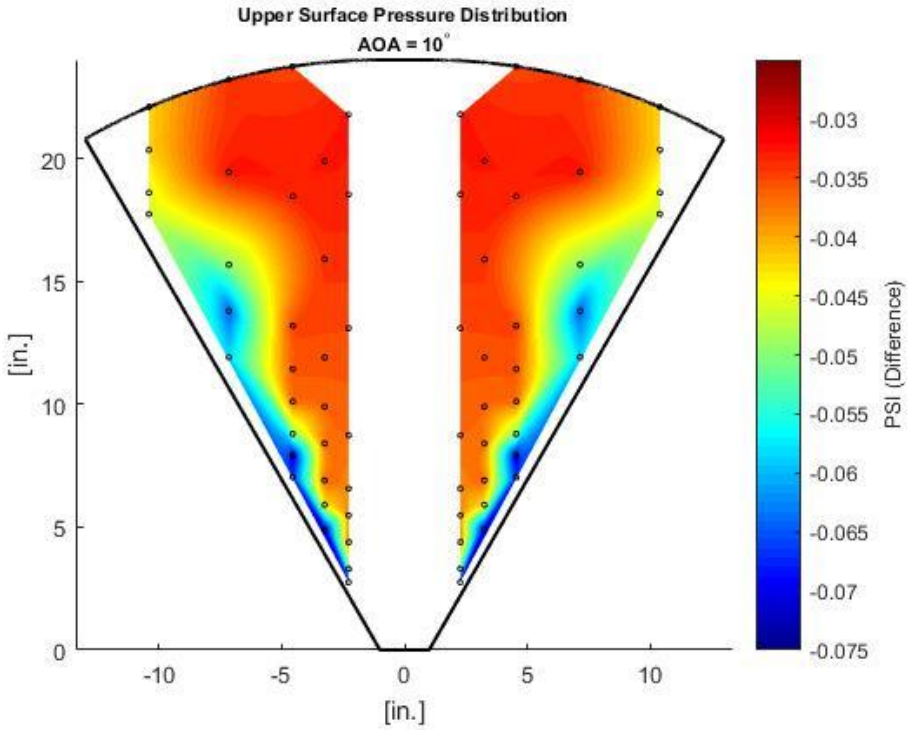

Figure 57: Λ = 60° | Upper Surface | α = 10° | Run 1

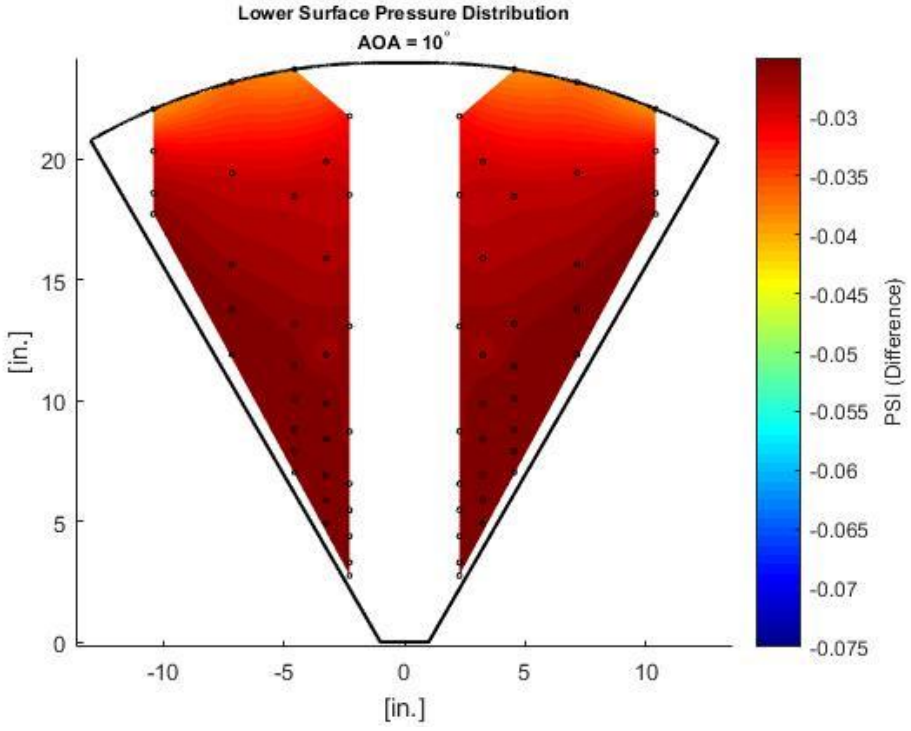

Figure 58: Λ = 60° | Lower Surface | α = 10° | Run 1

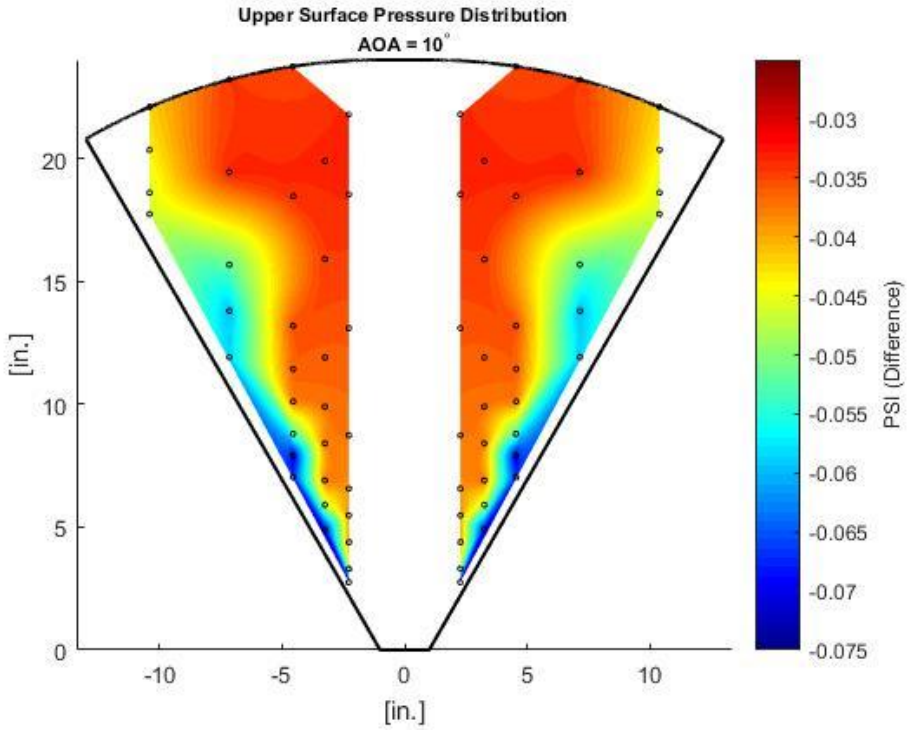

Figure 59: Λ = 60° | Upper Surface | α = 10° | Run 2

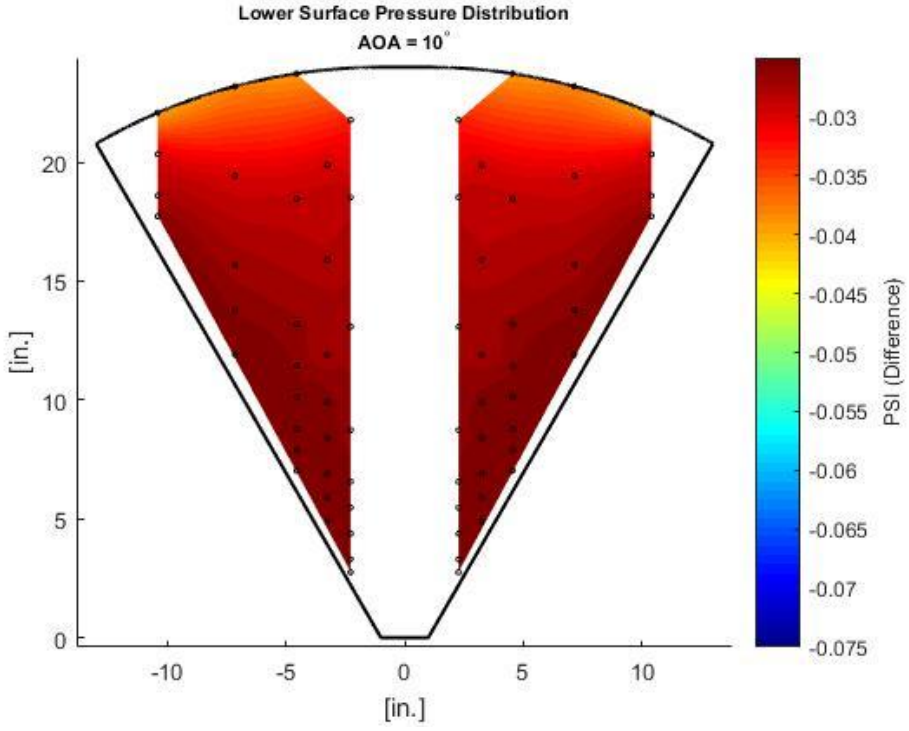

Figure 60: Λ = 60° | Lower Surface | α = 10° | Run 2

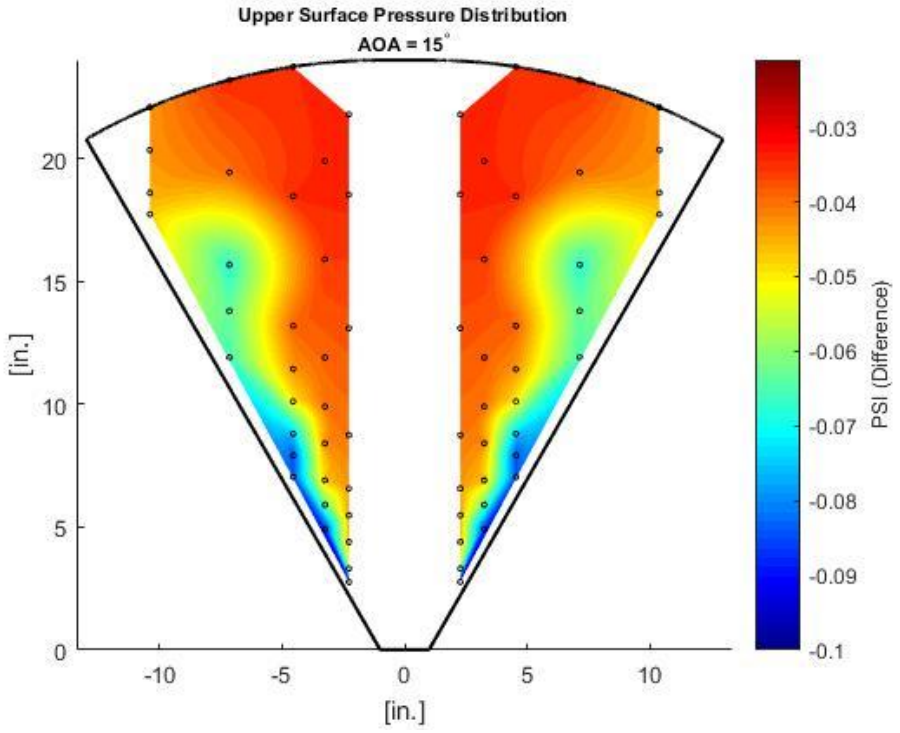

Figure 61: Λ = 60° | Upper Surface | α = 15° | Run 1

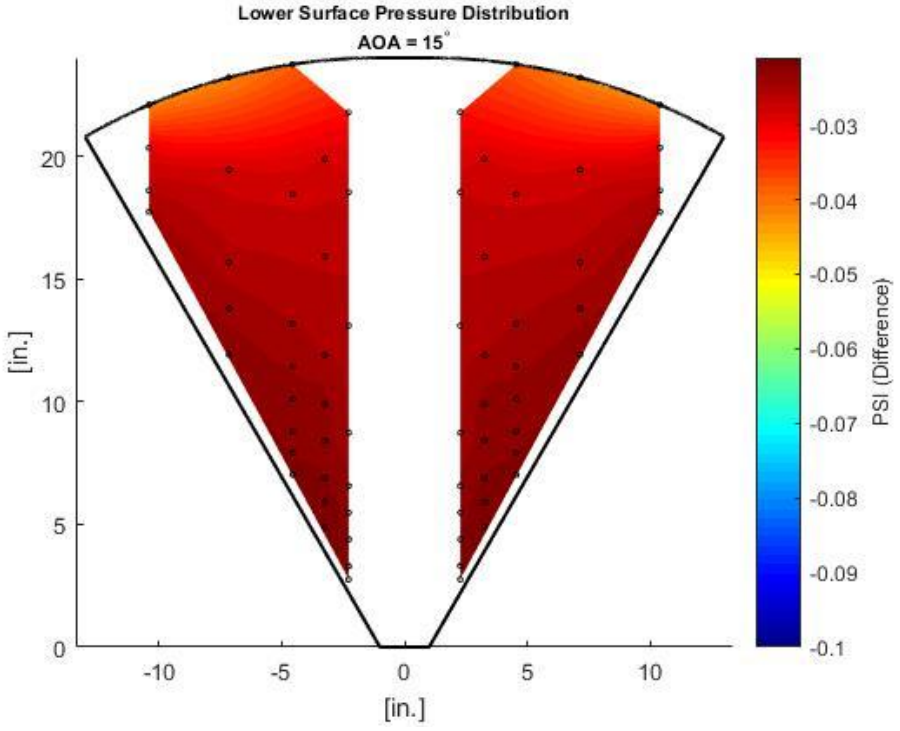

Figure 62: Λ = 60° | Lower Surface | α = 15° | Run 1

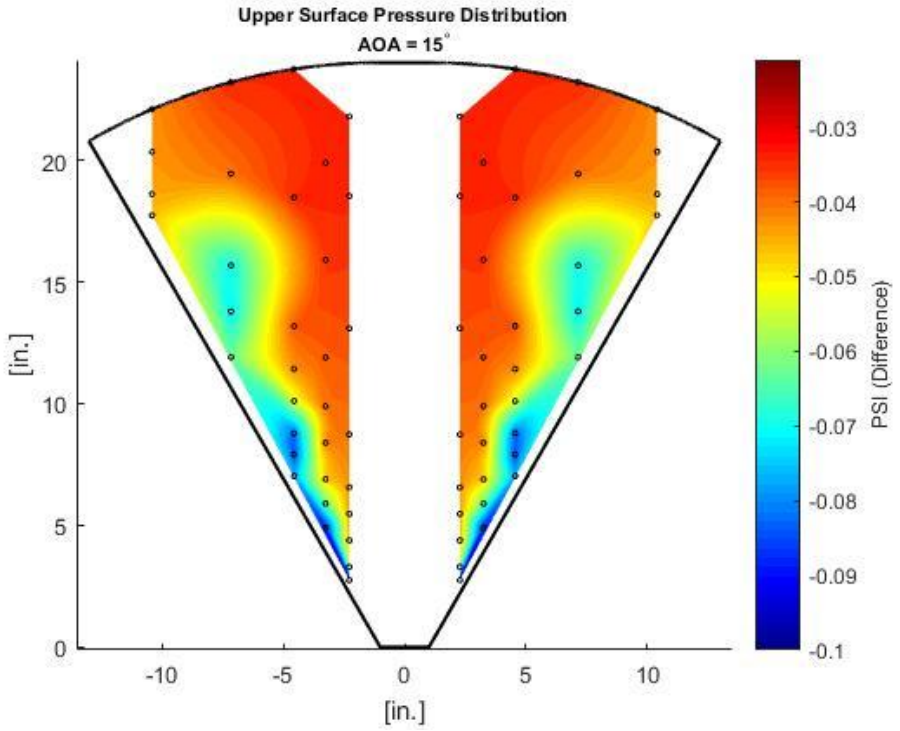

Figure 63: Λ = 60° | Upper Surface | α = 15° | Run 2

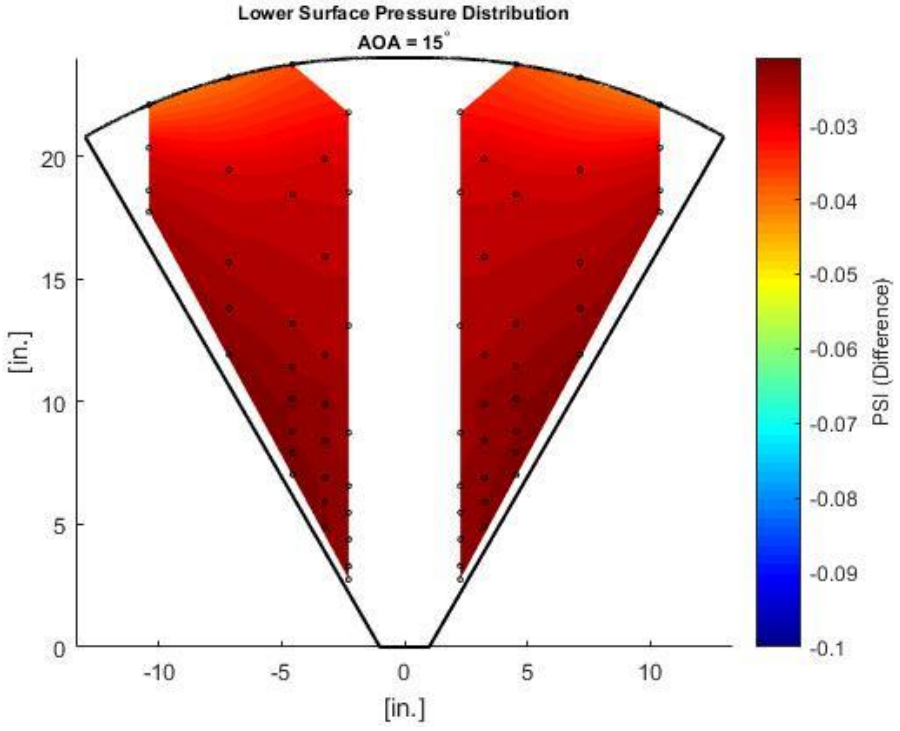

Figure 64: Λ = 60° | Lower Surface | α = 15° | Run 2

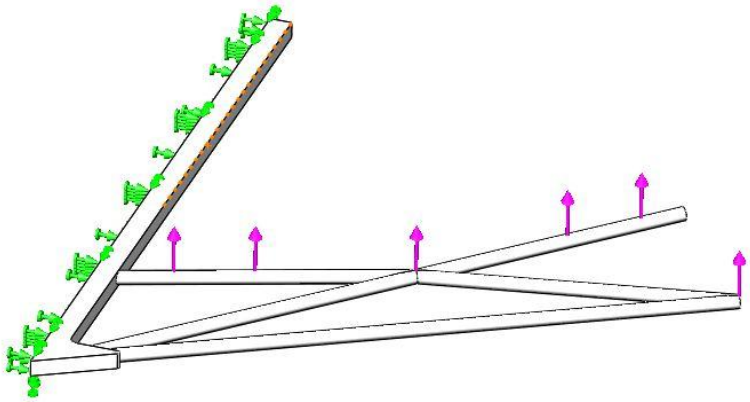

Figure 65: Boundary Conditions Applied to 45/15 Model

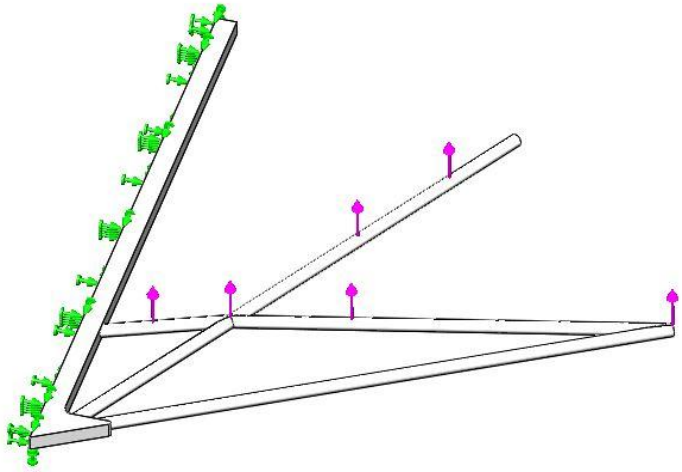

Figure 66: Boundary Conditions Applied to 30/30 Model

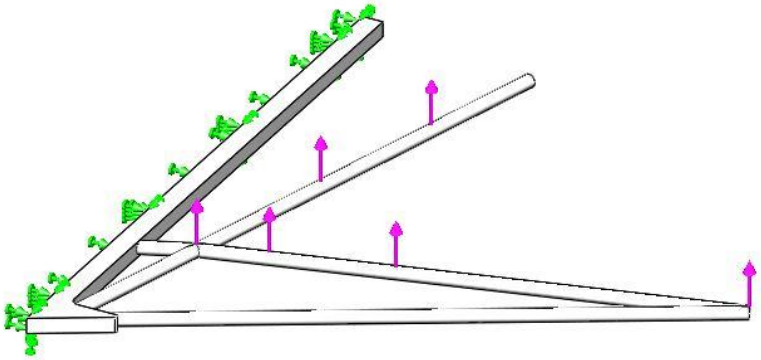

Figure 67: Boundary Conditions Applied to 15/45 Model

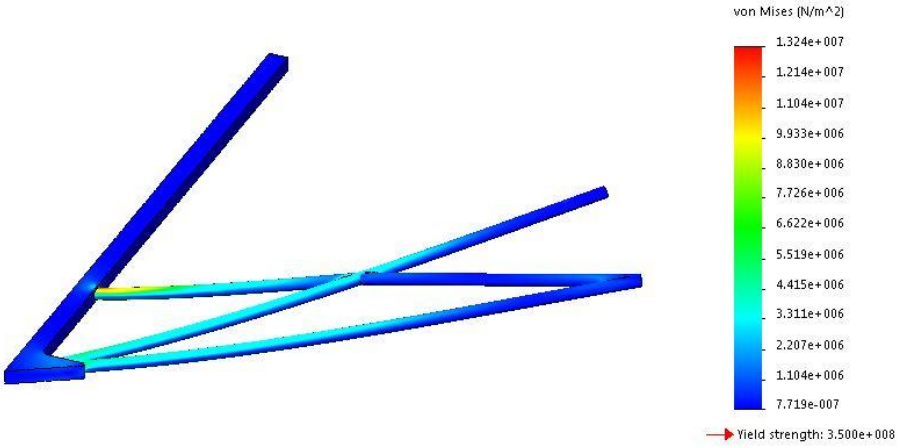

Figure 68: von Mises Stress | 45/15 Model | 15° AOA

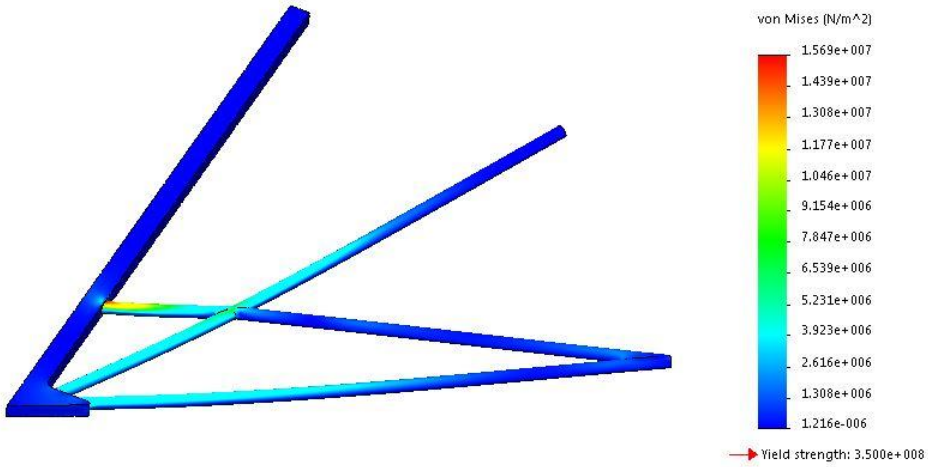

Figure 69: von Mises Stress | 30/30 Model | 15° AOA

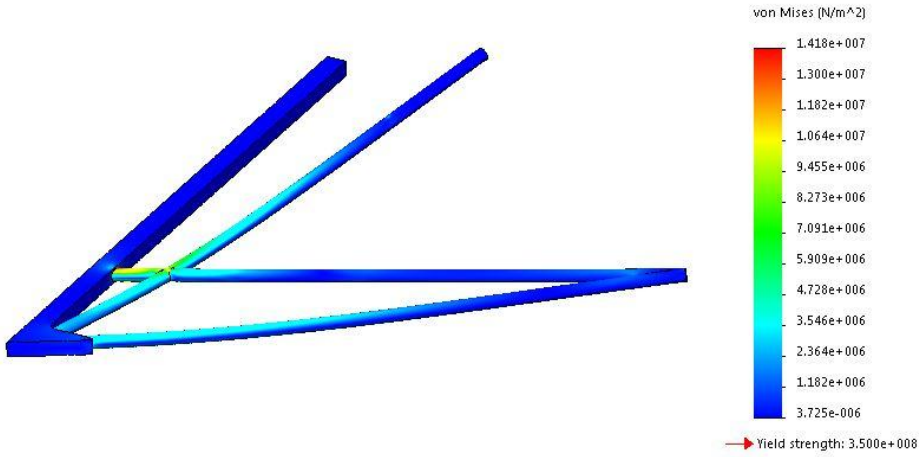

Figure 70: von Mises Stress | 15/45 Model | 15° AOA

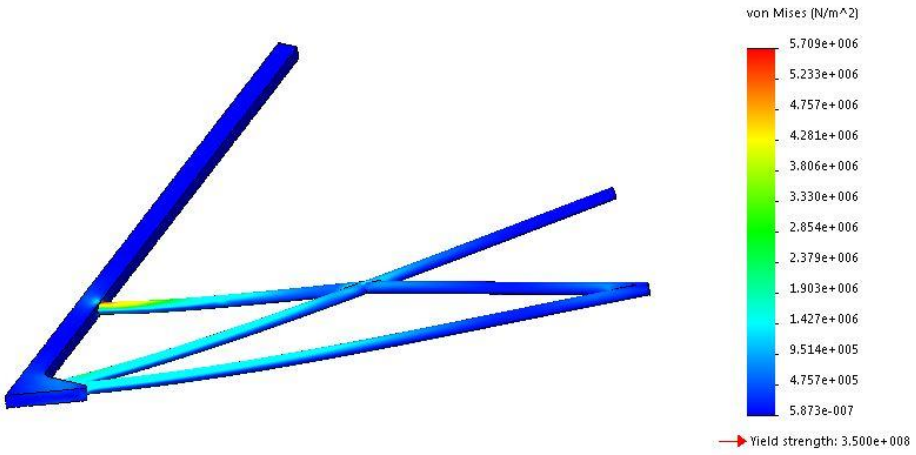

Figure 71: von Mises Stress [Pa] | 45/15 Model | 10° AOA

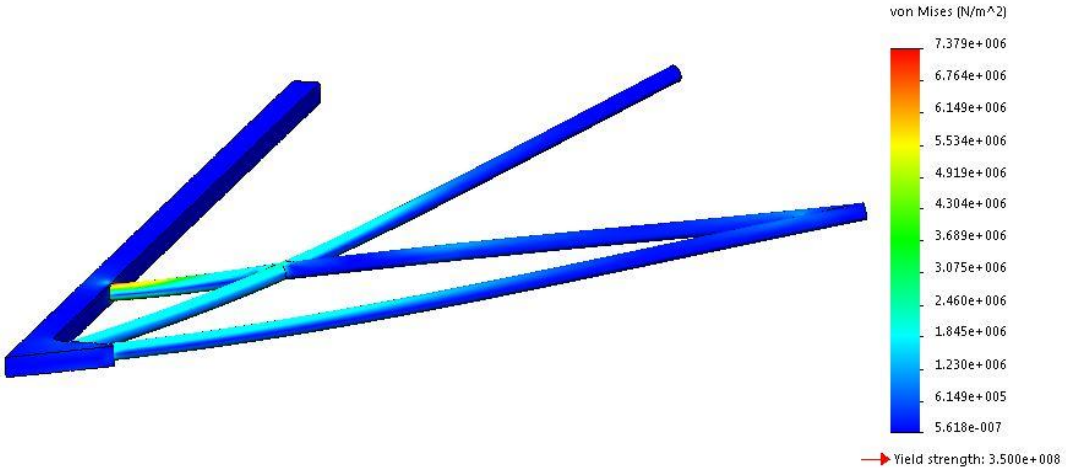

Figure 72: von Mises Stress [Pa] | 30/30 Model | 10° AOA

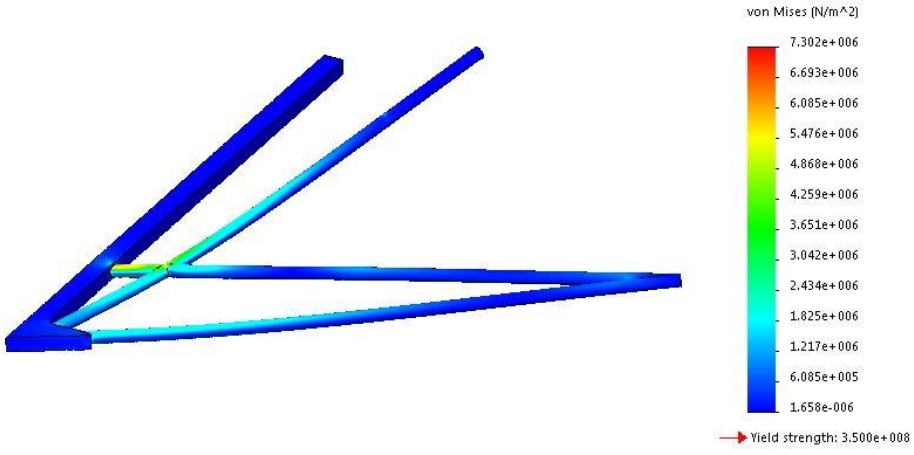

Figure 73: von Mises Stress [Pa] | 15/45 Model | 10° AOA

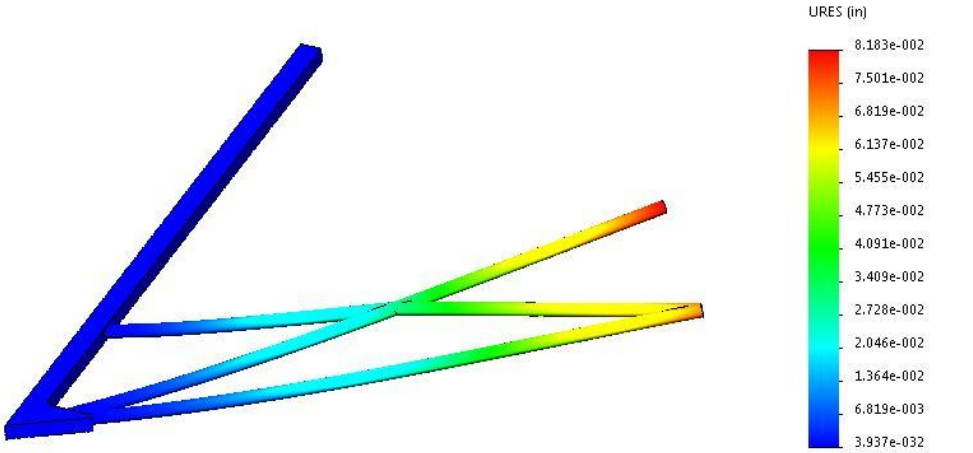

Figure 74: Displacement [in] | 45/15 Model | 10° AOA

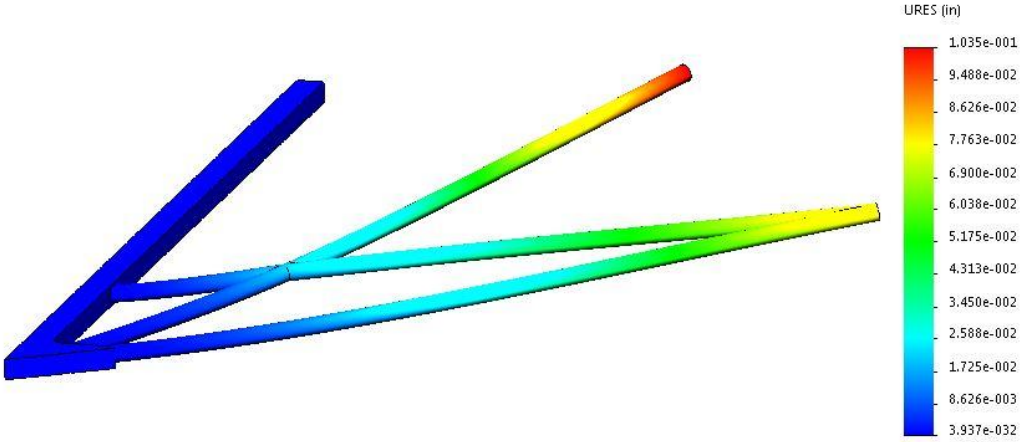

Figure 75: Displacement [in] | 30/30 Model | 10° AOA

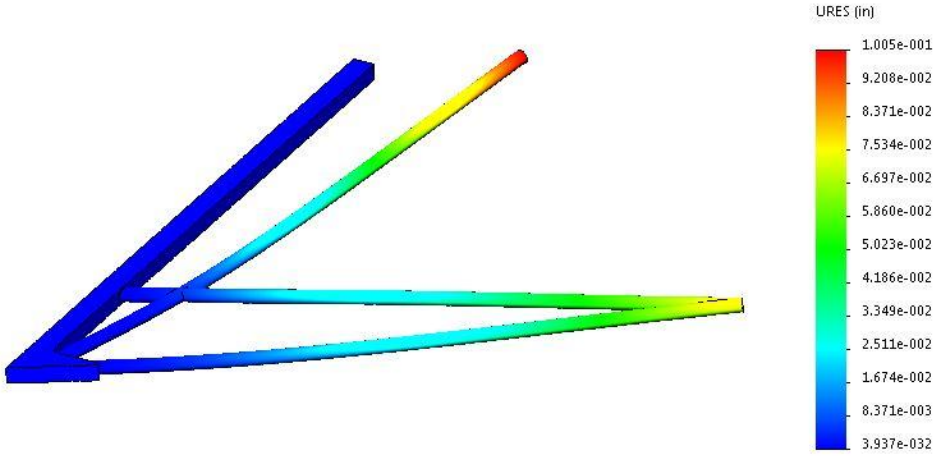

Figure 76: Displacement [in] | 15/145 Model | 10° AOA